SCIENCE CHINA Materials

REVIEW

mater.scichina.com link.springer.com

Published online 23 October 2015 | doi: 10.1007/s40843-015-0091-9
Sci China Mater 2015, 58: 819–850

Lanthanide-doped semiconductor nanocrystals: electronic structures and optical properties

Wenqin Luo[1,2], Yongsheng Liu[1] and Xueyuan Chen[1*]

Trivalent lanthanide (Ln^{3+}) ions doped semiconductor nanomaterials have recently attracted considerable attention owing to their distinct optical properties and their important applications in diverse fields such as optoelectronic devices, flat plane displays and luminescent biolabels. This review provides a comprehensive survey of the latest advances in the synthesis, electronic structures and optical spectra of Ln^{3+} ions in wide band-gap semiconductor nanocrystals (SNCs). In particular, we highlight the general wet-chemical strategies to introduce Ln^{3+} ions into host lattices, the local environments as well as the sensitization mechanism of Ln^{3+} in SNCs. The energy levels and crystal-field parameters of Ln^{3+} in various SNCs determined from energy-level-fitting are summarized, which is of vital importance to understanding the optical properties of Ln^{3+} ions in SNCs. Finally, some future prospects and challenges in this rapidly growing field are also proposed.

INTRODUCTION

Trivalent lanthanide ions (Ln^{3+}) possess fascinating optical properties and have been utilized in solid-state lasers, luminescent lamps, optical fibers, flat displays and other photonic devices for decades [1–10]. The emissions of Ln^{3+} ions mostly come from their intra 4f electronic transitions. Among Ln^{3+} series from La^{3+} to Lu^{3+}, each has its unique electronic structure and characteristic spectral signature, and thus multiple color outputs from visible to near infrared (NIR) can be achieved by doping with different Ln^{3+} ions, which is appealing for their technology applications. Moreover, because the 4f orbitals of Ln^{3+} are shielded by the filled $5s^25p^6$ sub-shells and prevented from the interaction with ligands, the emission features of Ln^{3+} vary little at different hosts. It should be noted that the inter-configuration of 4f electrons are parity forbidden, thus the photoluminescence (PL) of Ln^{3+} ions in various hosts is usually featured by sharp lines, long luminescent lifetime, and large Stokes/anti-Stokes shifts, which render the Ln^{3+} ions applicable in the fields of sensitive optical detectors and pure-color solid state lightings [11,12]. Nevertheless, due to the parity forbidden transition nature, the absorption cross-section of f-f transition is small and usually high power light sources such as laser are needed to excite the Ln^{3+} ions. The ability to excite Ln^{3+} ions efficiently in a broad spectral range is strongly desired for realizing their full potentials in signaling and lighting applications. To improve the excitation efficiency of Ln^{3+}, sensitization is an efficient way to avoid the direct excitation of the Ln^{3+}. Charge transfer, electronics transfer from ligand ground states (e.g., O 1s) to the Ln^{3+} excited states, has proved to be an efficient means to achieve intense Ln^{3+} emissions, due to its large band absorption cross-section. By employing this strategy, commercial phosphor Y_2O_3:Eu^{3+} has been demonstrated to be an excellent red phosphor, which can be effectively excited at Eu-O charge transfer band at 255 nm. Another strategy for efficient sensitization of Ln^{3+} is via the energy transfer (ET) from semiconductor nanocrystals (SNCs), which generally possess large absorption cross-section for Ln^{3+} excited states. Moreover, it is known that the exciton Bohr radius of semiconductors is much larger than that of insulators [13], which could result in pronounced quantum confinement effect for small nanocrystals (NCs) (e.g., 2–10 nm for In_2O_3, ZnO and TiO_2). As a result, the optical properties of Ln^{3+} incorporated in SNCs could be tailored via size control or bandgap engineering, which is very attractive in fabricating a nano-device for technological applications. It is anticipated that the luminescence of Ln^{3+} ions can be efficiently sensitized via the energy transfer from the excited host to Ln^{3+}, which thereby overcomes the inefficient direct absorptions of the parity forbidden 4f-4f transitions of Ln^{3+} ions (Fig. 1). To realize the efficient energy transfer and intense Ln^{3+} PL, the successful incorporation of Ln^{3+} into the lattices of SNCs is of utmost importance, which still remains a great challenge via conventional wet-chemical methods especially for some widely used wide bandgap

[1] Key Laboratory of Optoelectronic Materials Chemistry and Physics, Fujian Institute of Research on the Structure of Matter, Chinese Academy of Sciences, Fuzhou 350002, China
[2] College of Life Sciences, Huzhou University, Huzhou 313000, China
[*] Corresponding author (email: xchen@fjirsm.ac.cn)

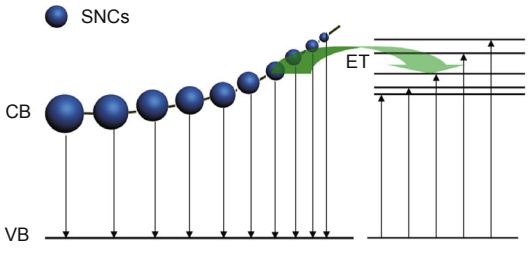

Figure 1 A schematic illustration of quantum size effect on the bandgap energy of SNCs and energy transfer mechanism from SNCs to Ln^{3+} ions.

SNCs with large discrepancy of ionic radius and charge between Ln^{3+} and the host cations such as ZnO, ZnS, CdS [14]. In spite of this, considerable efforts have been devoted to the synthesis and optical property tuning in Ln^{3+} ions doped SNCs in the past few years [15–34]. Although, in most cases reported in the literature [35–39], only broad emission lines of Ln^{3+} ions located at the surface of SNCs were obtained, it proved that Ln^{3+} can be incorporated into the SNC lattice site via judiciously designing the synthesis strategies. Diverse Ln^{3+} ions have been successfully embedded into the lattices of SNCs such as ZnO, TiO_2, SnO_2, In_2O_3, and Ga_2O_3 via various wet-chemical methods. As a result, intense and sharp emission lines of Ln^{3+} ions ranging from visible to NIR regions were realized in most SNCs via host sensitization. Moreover, multiple sites of Ln^{3+} with different crystal-field (CF) surroundings could be explicitly identified in various SNCs by using site-selective and time-resolved spectroscopy. Based on the abundant experimental CF levels of multiplets of Ln^{3+} ions within the SNC lattice sites identified from the highly resolved and intense emission and excitation lines of Ln^{3+}, many efforts had been devoted to the energy level fitting and thus to explore the CF surroundings experienced by the Ln^{3+} ions. As a consequence, the obtained CF parameters are particularly important in optimizing optical performance for further technological applications of the materials.

Previously, the optical properties of Ln^{3+} in SNCs were occasionally summarized in several reviews [40–43]. However, a comprehensive survey covering the preparation strategy, optical properties, and electronic structures of Ln^{3+} in SNCs is still lacking so far. This review mainly concentrates on the electronic structures and optical properties of Ln^{3+} ions doped in SNCs that were synthesized by using various methods. It is organized as follows. First, the most representative synthetic strategies to prepare SNCs with Ln^{3+} embedded in the host lattice site are briefly introduced. Then, the CF structures of Ln^{3+} ions in SNC lattice sites derived from the energy level fitting are summarized and discussed. Finally, the doping locations and the host sensitized luminescence of Ln^{3+} ions in SNCs are probed and revealed.

SYNTHESIS TECHNIQUES

To realize efficient energy transfer from host materials to Ln^{3+} ions, the distance between energy donor and acceptor should be small enough (usually less than 5 nm). To meet this requirement, it is essential to incorporate Ln^{3+} ions into the SNCs lattice. It is well known that the dopant situation in a host is closely related to the ionic radius and charge difference between dopant ions and host cations. For III-VI SNCs, such as In_2O_3 and Ga_2O_3, the Ln^{3+} dopant ions and host cations have similar ionic radius and the same charge. Thus In_2O_3 SNCs with Ln^{3+} ions embedded in the host lattice can be easily obtained by chemical methods [44]. However, for II-VI and IV-VI SNCs, such as ZnO, ZnS, and TiO_2, due to the large mismatch in ionic radius between Ln^{3+} and host ions (e.g., 0.086–0.103 nm *vs.* 0.061 nm for Ti^{4+}, for coordination number VI) [45] and their charge imbalance, it is notoriously difficult to incorporate Ln^{3+} ions into the SNCs lattice through conventional chemical methods. To this end, diverse chemical and physical methods had been attempted to synthesize Ln^{3+} doped SNCs as briefly reviewed in Table 1. In some special cases, it was found that, Ln^{3+} ions could be effectively incorporated into a metastable lattice site of SNCs usually accompanied with lattice distortion and charge compensation.

To effectively incorporate Ln^{3+} ions into SNC lattice site via wet chemical approach, it is essential to retain the dopant ions within the SNC matrix during the nanocrystal growth process. Sol-gel process has proved to be an effective way to capture the Ln^{3+} ions. During the hydrolysis process of the precursor molecules, Ln^{3+} ions can be readily bonded to the host ionic ions via oxygen bridges. With the particle growth, Ln^{3+} ions can be embedded into the host matrix (Fig. 2a). However, it should be noted that the as-prepared NCs by sol-gel method are usually in amorphous nature, and post heat treatment is thus needed to yield crystallized samples. In this case, lanthanide ions are thermally metastable in the glassy host matrix, and careful heat treatment should be conducted since high-temperature annealing may result in self-purification process and thus Ln^{3+} ions might be expelled from the crystallized lattice and form separated phase [46].

Another approach to increase the contents of Ln^{3+} ions in the host crystal lattice is shell overgrowth, which was successfully applied to increase doping level of transition metal and Ln^{3+} ions in SNCs [168–171]. By epitaxial growth of additional layers of host material, the surface dopant ions will be transferred to the lattice sites (Fig. 2b). Recently,

Table 1 Typical approaches for the synthesis of Ln^{3+} doped SNCs

Host	Ln^{3+}	Preparation method	Ref.
	II-VI		
ZnO	Eu, Er	Hydrothermal	[22,48,49]
	Dy, Tb, Er	Isocrystalline core-shell (ICS) protocol	[51]
	Eu	Electrochemical deposition	[55]
	Pr, Sm, Tb, Ho, Tm, Eu	Sol-gel	[17,57–59]
	Er, Eu	Chemical combustion	[64,65]
	Eu	Co-decomposition	[38]
	Eu	Thermal evaporation	[68]
	Tm	Implantation	[72]
	Eu	Solid state chemical reaction	[73]
	Eu	Microemulsion	[80]
	Er, Yb, Gd, Tb, Eu	Precipitation	[81,82]
	Tb, Eu	Polyol-mediated method	[86]
	Eu	Combustion	[88,89]
ZnS	Tb, Eu, Er, Yb, Gd	Precipitation	[25,26,91–94]
	Eu	Colloid method	[97]
	Er	Thermal evaporation	[101]
	Tm,Er	Ion implantation	[106]
	Tb,Eu	Post synthetic modification	[27]
CdS	Eu,	Co-precipitation	[112–114]
	Eu	Solvothermal	[117]
	Sm, Pr, Eu	Sol-gel	[119–122]
	IV-VI		
TiO_2	Eu, Tb, Sm, Er, Yb	Sol-gel (solvothermal)	[124–136]
	Eu	Surfactant-assisted synthesis	[151]
	Er^{3+}, Nd^{3+}, Yb^{3+}, Eu^{3+}	Thermal decomposition	[153]
	Er, Yb, Eu, Sm	Hydrothermal	155–158
	Sm	Soft chemical	[160]
	Sm	Laser ablation	[162]
	Eu	Ar/O_2 radio-frequency thermal plasma	[23,164–166]
	Eu, Tb, Nd	Magnetron sputtering	[167]
ZrO_2	Er, Yb	Complex precursor method.	[47]
	Er	Atomic layer deposition	[50]
	Eu, Pr	Hydrothermal	[52–54]
	Er	Ligand-capped/ligand-exchanging	[56]
	Dy, Yb, Pr, Sm, Er	Sol-gel	[60–63]
SnO_2	Nd	Deposition	[66]
	Eu	Impregnation and decomposition cycle	[67]
	Er, Eu,	Solvothermal	[69–71]
	Eu	Microwave synthesis	[21]
	Er, Yb, Eu	Sol-gel	[74–79]
	III-VI		
Ga_2O_3	Er, Eu,	Combustion	[83–85]
	Eu	Electrospinning	[87]
	Dy	Soft-chemical method	[90]
	Eu, Tb	Solvothermal	[95,96]
	Eu, Er, Dy	Solid state reaction	[98–100]
	Eu, Dy,	Sol-gel	[102–105]
	Eu	Spray pyrolysis	[107,108]
In_2O_3	Eu, Er,	Sol-gel	[109–111]
	Eu, Er, Yb	Solvothermal	[44,115,116]
	Eu	Melt quenching	[118]
	III-V		
GaN	Eu	Organometallic vapor phase epitaxy	[123]
	Eu, Sm	Molecular beam epitaxy	[137–150]
	Eu	Ion-implanted	[152]
	Eu, Tb	Thermal decomposition	[154]
	Eu	Solid state reaction	[159]
AlN	Sm, Dy, Tm,	Radio-frequency magnetron reactive sputtering	[161]
	Sm	CVD	[163]

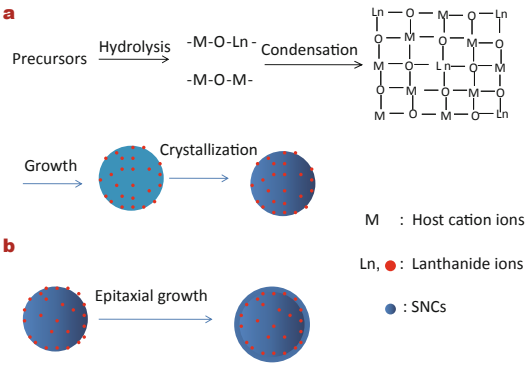

Figure 2 A schematic illustration of the strategies to incorporate Ln^{3+} ions into the SNC lattice through (a) sol-gel, and (b) epitaxial growth method.

Martin-Rodriguez and co-workers [171] presented a facile way to incorporate Yb^{3+} ions into the CdSe quantum dots (QDs) through epitaxial growth method, and enhanced energy transfer from CdSe host to Yb^{3+} ions was achieved. As shown in Fig. 3a, CdSe QDs were used as core templates, and the Yb and Se were then successively coated onto the CdSe QDs surface. During the shell growth process at high temperature of 265°C, the Yb^{3+} ions can diffuse into the CdSe host lattice. During the doping process, the morphology and dispersity of the nanoparticles can be retained (Fig. 3b). Fig. 3c shows the PL excitation and emission spectra of CdSe:Yb^{3+} NCs. For the sample with Yb^{3+} physically adsorbed on the surface, energy transfer from CdSe to Yb^{3+} can be obtained, and thus broad emission band at around 980 nm attributed to the $^2F_{5/2}$ to $^2F_{7/2}$ transition of Yb^{3+} was observed (Fig. 3d). Such surface adsorbed Yb^{3+} ions were unstable and easily desorbed from the nanoparticle after washing, which resulted in the decrease of emission intensity of Yb^{3+}. Followed by the coating of Se layer, the emission lines of Yb^{3+} ions became sharper and better resolved (Fig. 3e), indicating that the Se coating promoted the incorporation of Yb^{3+} in CdSe QDs. Meanwhile, the PL decay curve of CdSe:Yb^{3+} QDs also provided additional evidence for the incorporation of Yb^{3+} in CdSe lattice. As shown in Fig. 3f, the PL lifetime of $^2F_{5/2}$ of Yb^{3+} was found to be significantly prolonged after Se layer growth due to the minimization of surface quenching groups such as C–H (~3000 cm^{-1}) or O–H (~3300 cm^{-1}) by doping into the CdSe lattice site.

ELECTRONIC STRUCTURES OF LANTHANIDE IONS IN SNCs

Crystal-field theory of Ln^{3+}

The electronic structure of Ln^{3+} is closely related to their locations in the host [172]. A slight variation of local structure around Ln^{3+} ions will lead to a significant change in the CF of Ln^{3+}. It is a general practice to perform the energy-level-fitting by the parameterization of an effective operator Hamiltonian including free-ion (FI) and CF interactions. The commonly used effective operator Hamiltonian is

$$H = H_{\mathrm{FI}} + H_{\mathrm{CF}}, \tag{1}$$

where the FI Hamiltonian can be expressed as

$$H_{\mathrm{FI}} = E_{\mathrm{avg}} + \sum_{k=2,4,6} F^k f_k + \zeta_f A_{\mathrm{SO}} + \alpha L(L+1) + \beta G(R_2) + \gamma G(R_7) + \sum_{i=2,3,4,6,7,8} T^i t_i + \sum_{h=0,2,4} M^h m_h + \sum_{f=2,4,6} P^f p_f. \tag{2}$$

There are up to 20 FI parameters in Equation (2). The predominant terms in this Hamiltonian are the electrostatic and spin-orbit interactions represented by parameters F^k and ζ_f. The configuration interactions (α, β, γ), spin-spin and spin-other-orbit interactions (M^h), the two-body electrostatically correlated magnetic interactions (P^f), and the three-particle configuration interactions (T^i) represent higher order interactions that are essential in order to accurately reproduce the energy level structure of *f*-element ions. The physical meaning of these FI parameters has been described by Crosswhite and Carnall *et al.*[173,174].

The single-particle CF Hamiltonian is expressed in Wybourne's notation [175],

$$H_{\mathrm{CF}} = \sum_{k,q} \mathrm{Re}\, B_q^k [C_q^k + (-1)^q \cdot C_{-q}^k] + i\, \mathrm{Im}\, B_q^k [C_q^k - (-1)^q \cdot C_{-q}^k]. \tag{3}$$

The values of k and q are limited by the site symmetry of Ln ions, since the Hamiltonian must be invariant under the operations of the point group symmetry. In the low site symmetry, all the independent CF parameters except B_o^k are complex, each having real and imaginary parts denoted by $\mathrm{Re}B_q^k$ and $\mathrm{Im}B_q^k$. It should be noted that the CF parameters defined in Wybourne's notation are complex conjugate to their counterparts in Morrison's definition [176].

The scalar CF strength (S) that reflects the overall CF interaction in the crystal can be calculated according to Chang's definition [177]

$$S = \left\{ \frac{1}{3} \sum_{k=2,4,6} \frac{1}{2k+1} \left[\left| B_0^k \right|^2 + 2 \sum_{q>0} \left(\left| \mathrm{Re}\, B_q^k \right|^2 + \left| \mathrm{Im}\, B_q^k \right|^2 \right) \right] \right\}^{1/2}. \tag{4}$$

Ln^{3+} doped TiO_2 NCs

Eu^{3+}

The high-resolution site-selective PL excitation and emis-

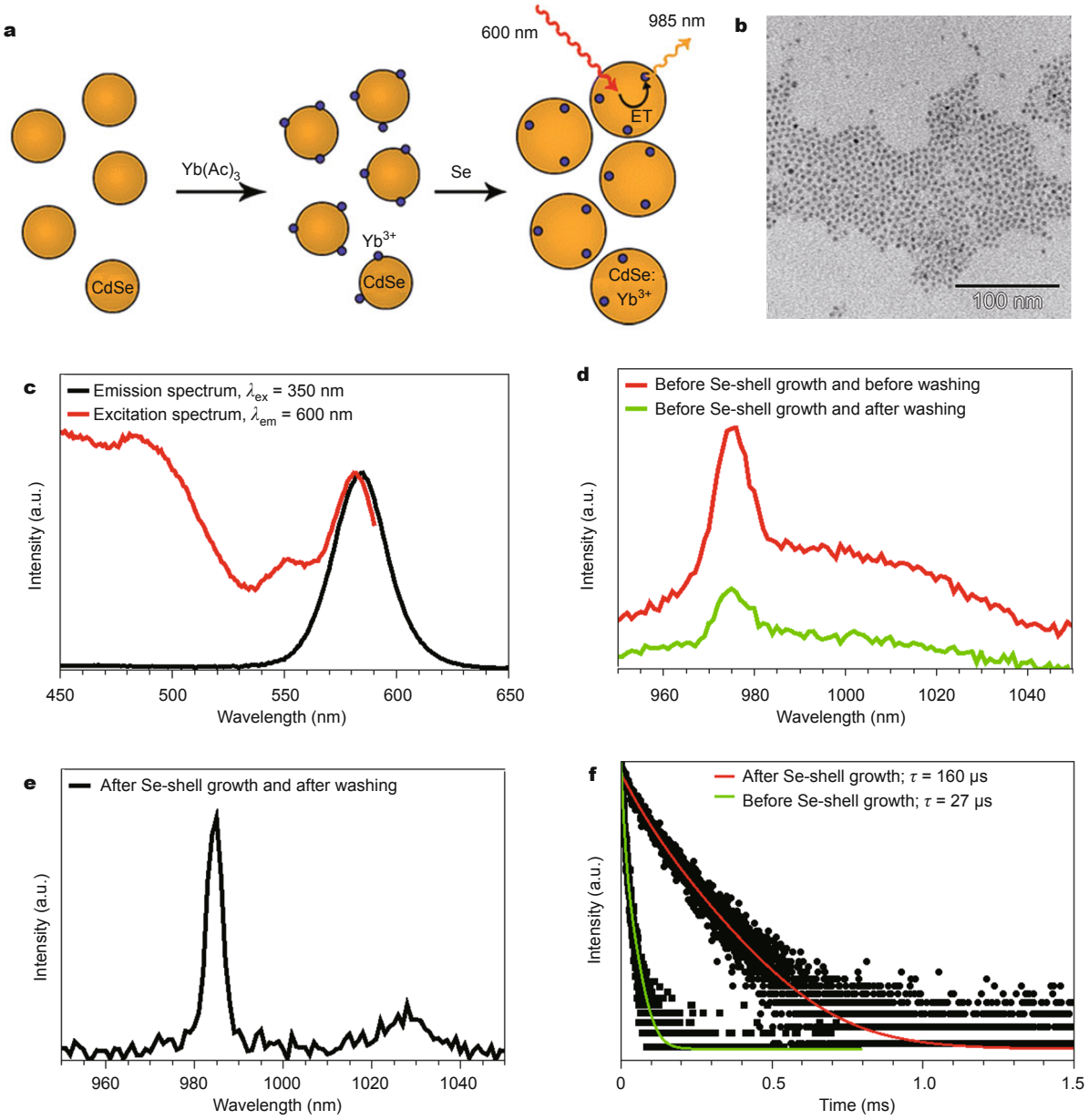

Figure 3 (a) A schematic illustration of the incorporation of Yb^{3+} ions into CdSe host lattice; (b) transmission electron microscopy (TEM) image of CdSe:Yb^{3+} QDs; (c) emission (λ_{ex} = 350 nm) and excitation (λ_{em} = 600 nm) spectra of CdSe:Yb^{3+}; (d) NIR emission spectra of unshelled CdSe:Yb^{3+} before (red line) and after (green line) washing; (e) PL emission spectrum of CdSe:Yb^{3+} after Se-shell growth upon excitation at 585 nm; (f) PL decay curves of Yb^{3+} in CdSe QDs by monitoring the emission at 980 nm upon pulsed excitation at 580 nm before (green) and after (red) Se-shell overgrowth. (Adapted with permision from Ref. [171]. Copyright 2013, American Chemical Society).

sion spectra of TiO_2:Eu^{3+} at 10 K, 47 CF levels at C_{2v} site and 42 CF levels at D_2 site were experimentally determined as listed in Table 2 [178]. Thereafter, the energy level fitting was performed by Ma *et al.* [179] by allowing the variation of both 9 CF parameters and FI parameters such as Slater integrals and spin-orbit coupling constant. The fitted energy levels are compared with the experimental values in Table 2. The root mean square (*rms*) deviation of the final fit is as small as 31.8 cm^{-1} and 33.7 cm^{-1} for C_{2v} and D_2 sites, respectively, which indicates a good agreement between the observed and the calculated sets. However, it should be pointed out that there are some large discrepancies between the experimental and fitted results as marked by star symbol in Table 2, which may be caused by the un-

Table 2 Energy levels of Eu^{3+} ions situated at the sites of C_{2v} and D_2 symmetries in anatase TiO_2 NCs (unit: cm^{-1}). Reprinted with permission from Ref. [179]. Copyright 2011, Elsevier B.V.

Multiplet	$E_{calc.}$	$E_{exp.}$	ΔE	$E_{calc.}$	$E_{exp.}$	ΔE	Multiplet	$E_{calc.}$	$E_{exp.}$	ΔE	$E_{calc.}$	$E_{exp.}$	ΔE
		C_{2v}			D_2				C_{2v}			D_2	
$^7F_0$	−18	0	18	−3	0	3		21,411	21,462	51	–	–	–
$^7F_1$	226	233	7	277	278	1	$^5D_3$	24,109	24,093	−16	24,028	24,031	3
	397	411	14	384	377	−7		24,144	24,157	13	24,059	24,087	28
	423	435	12	400	407	7		24,260	24,248	−12	24,181	24,184	3
$^7F_2$	739	668	−71*	697	677	−20	$^5L_6$	24,500	24,497	−3	24,400	24,406	6
	879	891	12	875	880	5		24,567	24,565	−2	24,550	24,566	16
	1092	1060	−32	1093	1070	−23		24,656	24,655	−1	24,804	24,781	−23
	1226	1222	−4	–	–	–		24,871	24,882	11	24,907	24,904	−3
$^7F_3$	1801	1819	18	1842	1805	−37		25,107	25,143	36	25,048	25,065	17
	1909	1956	47*	1873	1865	−8		25,244	25,186	−58*	25,053	25,107	54*
	1954	1994	40	1949	1966	17		25,341	25,268	−73*	–	–	–
	2037	2027	−10	1960	1980	20		25,582	25,592	10	–	–	–
	2048	2069	21	2081	2069	−12	$^5L_7$	25,695	25,696	1	25,182	25,190	8
	–	–	–	2404	2411	7		25,909	25,920	11	25,662	25,603	−59*
$^7F_4$	2460	2449	−11	2585	2596	11		–	–	–	25,862	25,837	−25
	2658	2618	−40	2669	2663	−6		–	–	–	26,001	26,016	15
	2855	2860	5	2931	2952	21		–	–	–	26,472	26,469	−3
	2929	2951	22	3088	3116	28	$^5G_2$	–	–	–	25,941	25,925	−16
	3061	3072	11	3136	3131	−5	$^5G_3$	25,979	25,991	12	25,511	25,504	−7
	3142	3114	−28	–	–	–		26,081	26,099	18	–	–	–
	3186	3157	−29	–	–	–		26,171	26,184	13	–	–	–
$^5D_0$	17,081	17,107	26	17,020	17,063	43	$^5G_4$	26,454	26,464	10	–	–	–
$^5D_1$	18,836	18,828	−8	18,745	18,787	42	$^5G_5$	26,273	26,263	−10	26,282	26,299	17
	18,877	18,861	−16	18,788	18,798	10		26,372	26,391	19	–	–	–
	18,900	18,871	−29	18,914	18,806	−108*		26,527	26,535	8	–	–	–
$^5D_2$	21,278	21,247	−31	21,215	21,183	−32	$^5G_6$	–	–	–	26,182	26,172	−10
	21,386	21,403	17	21,317	21,341	24		–	–	–	–	–	–

certainty in the location of some energy levels due to the spectral overlap of three site emissions in some wavelength region under the current experimental conditions. Table 3 lists the final FI and CF parameters of the fit. By adopting the CF parameters in Table 3, the value of S is determined to be 751 and 1095 cm^{-1} for Eu^{3+} ions at the C_{2v} and D_2 site in anatase TiO_2 NCs, respectively, which are slightly larger than that at the C_2 site of Gd_2O_3 and double of that at the C_{2v} site of LaF_3 [182], indicating the large CF experienced by Eu^{3+} in TiO_2. The relatively large CF strength may be due to the great lattice distortion and site symmetry descending at Ln^{3+} sites since a lower point-group symmetry occupied by Ln^{3+} ions in the host usually results in a larger CF strength [183].

Er^{3+}

Fine CF splittings experienced by Er^{3+} in anatase TiO_2 NCs were observed in high-resolution PL excitation and emission spectra at 10 K (Fig. 4). Fig. 4a exhibits the 10 K excitation spectrum for Er^{3+} doped TiO_2 NCs when monitoring the $^4S_{3/2}\rightarrow{}^4I_{15/2}$ emission at 566.5 nm. Abundant sharp excitation lines of Er^{3+} centered at 380.8, 407.8, 445.6, 454.6, 489.5, 523.5, and 550.5 nm are attributed to the transitions from the ground state of $^4I_{15/2}$ to the excited states of $^4G_{11/2}$, $^2H_{9/2}$, $^4F_{7/2}$, $^2H_{11/2}$, $^4S_{3/2}$ and $^4F_{9/2}$, respectively. Eight CF levels of $^4I_{15/2}$ were determined to be 0, 15, 95, 166, 210, 378, 454, and 504 cm^{-1} according to the $^4S_{3/2}\rightarrow{}^4I_{15/2}$ emission at 10 K (Fig. 4b). Theoretically, the multiplets of Er^{3+} at D_{2d} or lower symmetry sites should present J+1/2 lines due to the Kramers degeneracy for $4f^{11}$ configuration of Er^{3+} [184]. The enlarged excitation spectra at different spectral regions at 10 K (Figs 4c–h) reveal that the excitation lines of different multiplets agree well with the expected degeneracy, thus further verifying the single lattice site of Er^{3+} ions in TiO_2 NCs. Moreover, in addition to the excitation lines from the lowest CF level of $^4I_{15/2}$, a number of hot bands

Table 3 FI and CF parameters of Ln^{3+} in SNCs of TiO_2, In_2O_3, and Ga_2O_3 (unit: cm^{-1})

Parameter	Anatase TiO_2					Rutile TiO_2		In_2O_3	Ga_2O_3
	C_{2v}[a] (Eu^{3+})	D_2[a] (Eu^{3+})	C_{2v}[b] (Er^{3+})	D_{2d}[b] (Er^{3+})	D_{2d}[c] (Sm^{3+})	D_{2d}[c] (Sm^{3+})	D_{2h}[c] (Sm^{3+})	C_2[d] (Eu^{3+})	$C_{2/m}$[e] (Eu^{3+})
E_{avg}	63,614	64,718	35,567(17)	35,567(29)	–	–	–	6,2791(56)	63,304(15)
F^2	82,256	84,685	96,528(130)	96,509(229)	[79,805][g]	[79,805]	[79,805]	80,206(108)	81,280(57)
F^4	61,248	60,381	64,835(187)	64,902(278)	[57,175]	[57,175]	[57,175]	59,968(774)	61,647(93)
F^6	40,411	41,288	57,754(243)	57,740(403)	[40,250]	[40,250]	[40,250]	41,068(465)	40,535(53)
ζ	1324	1349	2365(4)	2364(6)	[176]	[176]	[176]	1313(3)	1319(1)
α	–	–	17.79	17.79	[20.16]	[20.16]	[20.16]	21.4	20.16
β	–	–	−580	−580	[−566.9]	[−566.9]	[−566.9]	−567	−567
γ	–	–	1800	1800	[1500]	[1500]	[1500]	1500	1500
T^2	–	–	620	620	[300]	[300]	[300]	300	300
T^3	–	–	48	48	[36]	[36]	[36]	40	40
T^4	–	–	100	100	[56]	[56]	[56]	60	60
T^6	–	–	−475	−475	[−347]	[−347]	[−347]	−300	−300
T^7	–	–	380	380	[373]	[373]	[373]	370	370
T^8	–	–	163	163	[348]	[348]	[348]	320	320
M^0	–	–	2.95	2.95	[2.6]	[2.6]	[2.6]	2.1	2.1
P^2	–	–	627	627	[357]	[357]	[357]	360	360
B_0^2	99	−24	45(147)	121(105)	−452	−886	546	−168(47)	41(46)
B_2^2	−721	446	152(105)	–	–	–	615	−806(27)	−625(31)
B_0^4	1079	−3733	2483(164)	3035(132)	2276	4870	−4806	−1206(21)	−988(48)
B_2^4	−707	−1945	−1050(156)	–	–	–	−759	Re: −1951(57) Im: −221(162)	Re: −397(89) Im: −1243(42)
B_4^4	−2414	1125	−481(176)	−423(215)	2030	1745	1417	Re: 1133(62) Im: −271(243)	Re: −165(71) Im: 223(48)
B_0^6	2092	−3916	−143(144)	−170(86)	674	960	−117	143(96)	−1096(84)
B_2^6	−1697	−1853	248(126)	–	–	–	–	Re: 452(68) Im: 465(101)	Re: −177(78) Im: −201(59)
B_4^6	1182	171	395(76)	314(82)	−211	−133	752	Re: 1124(68) Im: −313(219)	Re: 73(93) Im: 553(58)
B_6^6	1073	121	124(105)	–	–	–	−1086	Re: −30 (90) Im: −253(93)	Re: 720(53) Im: 151(166)
rms[f]	31.8	33.7	25.1	31.7	16.6	37.5	3.1	13.8	12.9
S/cm^{-1}	751	1095	549	609	–	–	–	790	546

a) Ref. [179]; b) Ref. [180]; c) Ref. [181]; d) Ref. [115]; e) Ref. [83]; the values in parentheses are errors in the indicated parameters which were freely varied in the fit. f) The *rms* deviation between the experimental and calculated energies was used as a figure of merit to describe the quality of a fit, with

$$rms = \sqrt{\sum (E_{exp} - E_{calc})^2 / (N - P)}$$

where N is the number of levels fit, and P is the number of parameters freely varied. g) The FI parameters in brackets were adopted from Sm^{3+} in LaF_3 crystals in Ref. [174] and fixed during the energy level fitting.

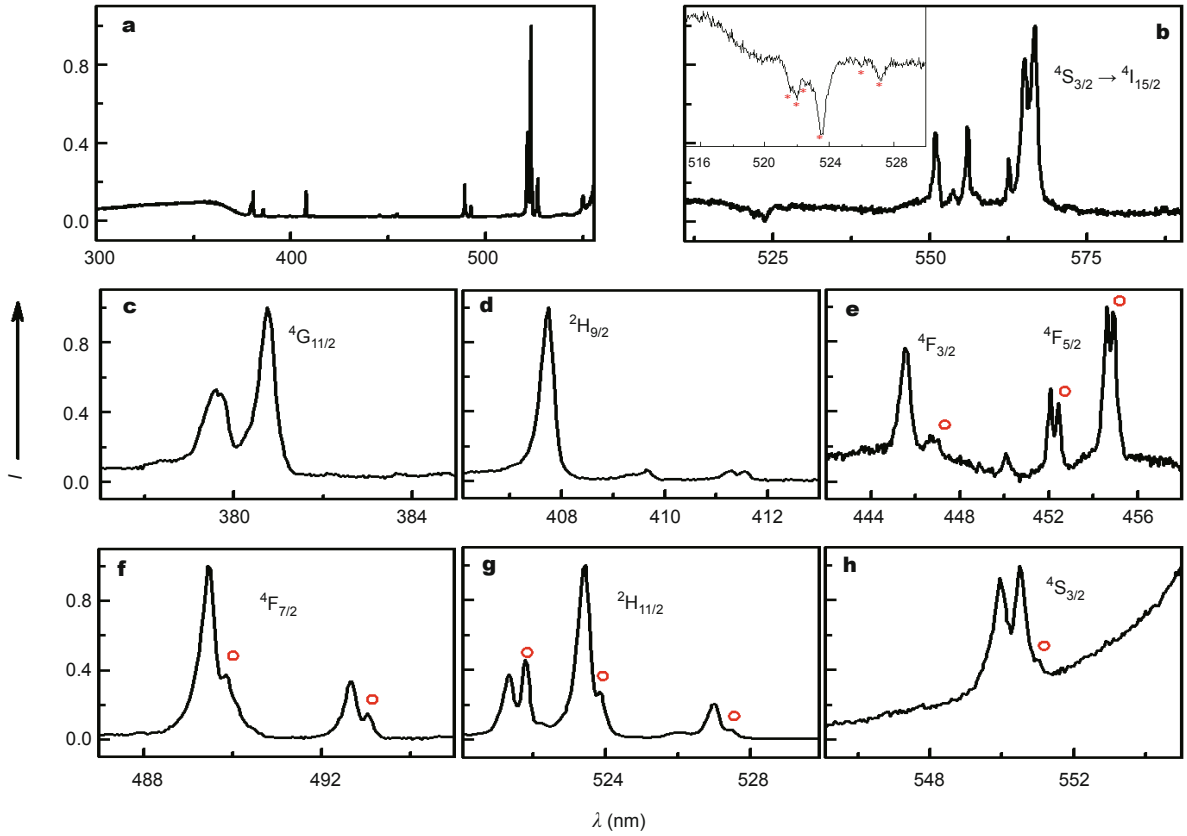

Figure 4 (a) 10 K PL excitation spectrum by monitoring the $^4S_{3/2} \rightarrow {}^4I_{15/2}$ emission at 566.5 nm; (b) PL emission spectra upon excitation at 407.8 nm for TiO_2:Er^{3+} NCs; (c–h) enlarged high-resolution excitation peaks in different spectral regions. Peaks marked by circles are hot bands from the second lowest level of the ground state. Reprinted with permission from Ref. [180]. Copyright 2011, Wiley-VCH Verlag GmbH & Co. KGaA.

marked by the circle symbols with an energy gap of 15 cm^{-1} appear in lower energy side, which are ascribed to the transitions from the second lowest CF level of $^4H_{15/2}$. From the viewpoint of spectroscopy, we infer that most of Er^{3+} ions are very likely located at the substitutional Ti^{4+} lattice site with a site symmetry descending from D_{2d} to C_{2v} or D_2, as previously revealed in Eu^{3+} doped TiO_2 NCs [178].

According to the high-resolution PL excitation and emission spectra at 10 K, 45 CF levels belonging to 12 different SLJ multiplets of $4f^{11}$ configuration of Er^{3+} were experimentally determined (Table 4) and subjected to energy level fitting [180]. The energy-level-fitting was performed using the *f*-shell empirical programs of Prof. Reid, which enabled a complete diagonalization without truncation of the $4f^{11}$ wave functions [185]. In the least-square fitting of CF energy level structure, five FI parameters (E_{avg}, F^k, ζ_f) were allowed to vary freely whereas the others of M^2, M^4, P^4, and P^6 were constrained by the Hartree-Fock-determined ratios M^2/M^0=0.56, M^4/M^0=0.38; P^4/P^2=0.75, P^6/P^2=0.5 [173]. The FI and CF parameters of LaF_3:Er^{3+} [174] were used as starting values. Some strategies were employed to fulfill the fit repeatedly: firstly, those most reliable CF levels were fitted by freely varying both the FI parameters (E_{avg}, F^k, ζ_f) and the CF parameters. The other FI parameters were fixed at the parameters of LaF_3:Er^{3+}; secondly, finely tuning the above fit by introducing the remaining FI parameters, or adding more CF levels of other multiplets such as those congested levels, or both; thirdly, relocating or reassigning those uncertain CF levels that would result in anomalously large *rms* deviation of the fit, and finally simultaneously varying the free parameters to fit the 45 CF levels. An *rms* deviation of 25.1 cm^{-1} based on the C_{2v} symmetry was obtained in the final fit, which is smaller than that based on the D_{2d} symmetry (31.7 cm^{-1}), indicating that the fitting based on C_{2v} is more reasonable in energy. The fitted energy levels for the D_{2d} and C_{2v} site symmetries are compared with experimental values in Table 4. The optimal FI and CF parameters are listed in Table 3. By adopting the CF parameters in Table 3, the value of *S* was determined to be 549 cm^{-1} for Er^{3+} ions at the C_{2v} site in anatase TiO_2 NCs,

Table 4 Energy levels of Er^{3+} at the D_{2d} and C_{2v} sites of TiO_2 NCs (unit: cm^{-1}). Reprinted with permission from Ref. [180]. Copyright 2011, Wiley-VCH Verlag GmbH & Co. KGaA

Multiplet	Energy			ΔE (D_{2d})	ΔE (C_{2v})	Multiplet	Energy			ΔE (D_{2d})	ΔE (C_{2v})
	Exp.	Fit (D_{2d})	Fit (C_{2v})				Exp.	Fit (D_{2d})	Fit (C_{2v})		
$^4I_{15/2}$	0	−1	−19	−1	−19		15,404	15,374	15,383	−30	−21
	15	19	7	4	−8	$^4S_{3/2}$	18,165	18,140	18,152	−25	−13
	95	74	81	−21	−14		18,183	18,184	18,195	1	12
	166	148	166	−18	0	$^2H_{11/2}$	18,975	18,997	18,972	22	−3
	210	223	219	13	9		19,010	19,089*	19,025	79	15
	378	401	392	23	14		19,104	19,112	19,086	8	−18
	454	446	469	−8	15		19,148	19,114	19,152	−34	4
	504	523	506	19	2		19,181	19,185	19,201	4	20
$^4I_{13/2}$	6525	6510	6525	−15	0		19,226	19,195	19,215	−31	−11
	6533	6542	6543	9	−10	$^4F_{7/2}$	20,298	20,342*	20,320	44	22
	6585	6599	6594	14	9		20,392	20,390	20,400	−2	8
	–	6620	6649	–	–		20,430	20,398	20,418	−32	−12
	–	6766	6745	–	–		20,466	20,459	20,453	−7	−13
	–	6820	6851	–	–	$^4F_{5/2}$	21,997	22,049*	22,049*	52	52
	–	6890	6859	–	–		22,119	22,109	22,117	−10	−2
$^4I_{11/2}$	–	10,155	10,166	–	–		22,217	22,178	22,161*	−39	−56
	–	10,189	10,184	–	–	$^4F_{3/2}$	22,386	22,384	22,381	−2	−5
	10,205	10,195	10,206	−10	1		22,444	22,440	22,452	−4	8
	–	10,276	10,268	–	–	$^2H_{9/2}$	24,298	24,274	24,283	−24	−15
	–	10,305	10,328	–	–		24,313	24,286	24,295	−27	−18
	–	10,354	10,330	–	–		24,411	24,414	24,406	3	−5
$^4I_{9/2}$	–	12,254	12,252	–	–		24,426	24,464	24,442	38	16
	–	12,288	12,287	–	–		24,525	24,547	24,546	22	21
	–	12,409	12,401	–	–	$^4G_{11/2}$	25,920	25,993*	25,991*	73	71
	–	12,472	12,453	–	–		26,062	26,049	26,031	−13	−31
	12,588	12,562	12,584	−26	−4		26,170	26,137	26,160	−33	−10
$^4F_{9/2}$	–	15,110	15,122	–	–		26,264	26,267	26,244	3	−20
	15,140	15,129	15,133	−11	−7		26,344	26,322	26,359	−22	15
	15,242	15,278	15,263	36	21		26,427	26,407	26,397	−20	−30
	15,291	15,316	15,303	25	12		–	–	–	–	–

which was close to that at the C_2 site in Y_2O_3 (S = 569 cm^{-1}) [177], but about two times that at the C_{2v} site in LaF_3 (S = 257 cm^{-1}) [186], indicative of a strong CF interaction experienced by Er^{3+}.

Sm^{3+}

Different from the multiple sites of Sm^{3+} in anatase TiO_2 NCs in our previous work [187], single lattice site of Sm^{3+} was detected in anatase TiO_2 NCs by Kiisk and co-workers [181], which enabled the precise assignment of experimental electronic state of Sm^{3+} in TiO_2 crystals. As shown in Fig. 5a, the shape and position of the emission lines are alike to that selected out under the excitation at 416.2 nm of Sm^{3+} in anatase TiO_2 prepared by sol-gel solvothermal method [187], indicative of the essentially same CF environment around Sm^{3+} in these two sites. Besides, well resolved emission lines of Sm^{3+} were also observed in rutile TiO_2 crystals (Fig. 5b), which exhibits significantly different emissive behavior from that of Sm^{3+} in anatase phase, indicative of the totally different local symmetry of Sm^{3+} in these two crystal phase.

In all, 16 energy levels belonging to ^6H_J (J= J=5/2, 7/2, 9/2, 11/2) multiplets of Sm^{3+} in anatase or rutile TiO_2 NCs were located and assigned as listed in Table 5. Due to the

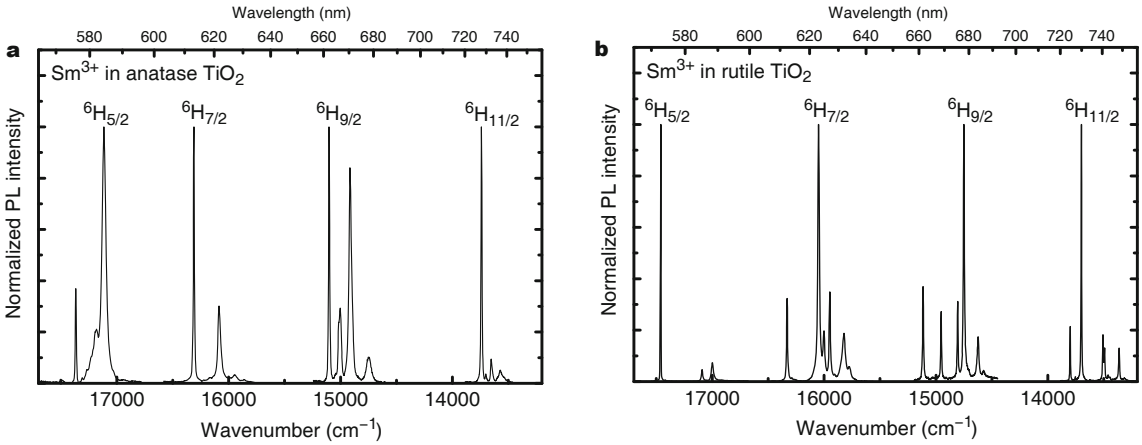

Figure 5 10 K high-resolution PL emission spectra of Sm^{3+} in (a) anatase and (b) rutile phase of TiO_2 under the excitation at 355 nm. The intensities of the bands corresponding to different multiplets were normalized at the most intense emission line. Reprinted with permission from Ref. [181]. Copyright 2009, IOP publishing Ltd.

Table 5 Calculated and observed energy levels of Sm^{3+} in anatase and rutile phases of TiO_2 (unit: cm^{-1}). Reprinted with permission from Ref. [181]. Copyright 2009, IOP publishing Ltd.

Multiplet	Anatase D_{2d}			Rutile D_{2d}			Rutile D_{2h}		
	$E_{exp.}$	$E_{calc.}$	ΔE	$E_{exp.}$	$E_{calc.}$	ΔE	$E_{exp.}$	$E_{calc.}$	ΔE
$^6H_{5/2}$	0	−24	24	0	71	−71	0	1	−1
	181	199	−18	376	312	64	376	375	1
	251	258	−7	469	458	11	469	469	0
$^6H_{7/2}$	1055	1067	−12	1135	1111	24	1135	1138	−3
	1204	1196	8	1415	1429	−14	1415	1415	0
	1280	1279	1	1514	1507	7	1514	1511	3
	1418	1415	3	1638	1659	−21	1638	1635	3
$^6H_{9/2}$	2265	2262	3	2348	2343	5	2348	2343	5
	2348	2330	18	2509	2503	6	2509	2509	0
	2364	2385	−21	2656	2656	0	2656	2656	0
	2451	2471	−20	2712	2691	21	2712	2716	−4
	2619	2598	21	2837	2870	−33	2837	2839	−2
$^6H_{11/2}$	3626	3635	−9	3663	3665	−2	3663	3664	−1
	3666	3657	9	3763	3806	−43	3763	3762	−1
	–	3698	–	–	3919	–	3964	3960	4
	3713	3706	7	3964	3927	37	–	4010	–
	3812	3818	−6	–	4083	–	4101	4105	−4
	–	3855	–	4101	4090	11	–	4228	–

small number of experimentally detected energy levels, the FI parameters were fixed at values provided in LaF_3 [174] during the energy-level-fitting. The fitted energy levels based on D_{2d} for anatase phase and D_{2d} or D_{2h} for rutile phase are compared in Table 5. The optimal CF parameters are listed in Table 3. By adopting the CF parameters in Table 3, the value of S was determined to be 609, 1033, and 1020 cm^{-1} for Sm^{3+} ions at the D_{2d} site of anatase, D_{2d} and D_{2h} sites of rutile TiO_2 NCs, respectively. It should be noted that the lattice distortion induced by the replacement of Ti^{4+} with larger Sm^{3+} and the charge compensation process was not taken into account in the energy level fitting, which

may be to some extent influence the final fitting results.

Ln^{3+} doped In_2O_3 NCs

Indium sesquioxide (In_2O_3) is a wide bandgap III-VI semiconductor (direct bandgap energy of ~2.9–3.2 eV) [188–190] with a large exciton Bohr radius of 2.14 nm [191]. Due to the similarity of ions radius and charge between In^{3+} and Ln^{3+} ions, Ln^{3+} ions can be easily incorporated into the In_2O_3 nanocrystal lattice by replacing In^{3+}. According to the crystal structure of In_2O_3 which crystallizes with the C-type Y_2O_3 structure, two distinct sites are expected for Ln^{3+} in the In-lattice, namely a low symmetry site of C_2 and a centrosymmetric site of S_6.

The optical properties of Ln^{3+} in In_2O_3 NCs have been sporadically reported in recent years [29,192–195]. Kim *et al.* [193] and Choi *et al.* [194] observed the Er^{3+} emission around 1.54 μm in In_2O_3:Er^{3+} under direct excitation of Er^{3+} ions. The Eu^{3+} luminescence was observed in In_2O_3:Eu^{3+} QDs upon indirect excitation above 350 nm at room temperature [29], due possibly to the host sensitization. Antic-Fidancev and co-workers [195] performed the energy-level-fitting of Eu^{3+} in C-type In_2O_3 polycrystals. 21 energy levels belonging to ^7F_J (J=0, 1, 2, 3, 4) multiplets of Eu^{3+} at the C_2 site of In_2O_3 were subjected to the fitting, yielding small *rms* deviation of 3.9 cm^{-1}. Recently, more elaborate spectroscopy and electronic structure analysis of Eu^{3+} in In_2O_3 NCs prepared by a solvothermal method were carried out in our group [115]. 48 CF levels below 25,500 cm^{-1} of Eu^{3+} at the C_2 site of In_2O_3 were located and assigned based on the 10 K high-resolution PL excitation and emission spectra. Fig. 6 presents the emission and excitation spectra of Eu^{3+} in In_2O_3 NCs. As shown in Fig. 6a, upon direct excitation from the ground state $^7F_0$ to $^5D_2$ of Eu^{3+} (C_2) at 465.1 nm, sharp emission lines corresponding to $^5D_1 \rightarrow {}^7F_1$ and $^5D_0 \rightarrow {}^7F_J$ (J = 0, 1, 2, 3, 4, 5, 6) transitions of Eu^{3+} were observed at 533.0, 580.4, 586.3, 611.0, 648.4, 709.4, 741.4 and 804.4 nm, respectively. Sharp excitation peaks centered at 467.4, 528.2 and 580.4 nm attributing to the direct excitation of Eu^{3+} from the ground state $^7F_0$ to different ^5D_J (J = 2, 1, 0) multiplets can be well assigned as illustrated in Fig. 6b. Furthermore, besides the direct excitation lines of Eu^{3+}, an intense broad UV band centered at 350 nm that originates from the bandgap absorption of In_2O_3 NCs is also presented in Fig. 6b, indicating that the Eu^{3+} emissions can be achieved via an efficient nonradiative energy transfer process from the In_2O_3 host to Eu^{3+}.

The energy-level-fitting was performed and the procedure is similar to that of TiO_2:Er^{3+}. The *rms* deviation of the final fit is only 13.8 cm^{-1}, indicative of excellent agreement between the experimental and fitted CF levels. The fitted energy levels are compared with experimental values in Table 6. The FI and CF parameters are listed in Table 3. The CF parameters of B_0^2, $\mathrm{Im}B_0^2$, B_0^6, $\mathrm{Im}B_2^6$, $\mathrm{Im}B_4^6$ and $\mathrm{Im}B_6^6$ are significantly different from that reported by Antic-Fidancev *et al.* [195], which is most probably due to much less experimental data (only 21 CF levels) included in their energy-level-fitting and thus the less reliability of the sixth-rank parameters than that of the second- and fourth-rank parameters. The obtained CF parameters are also compared with that of cubic Y_2O_3:Eu^{3+} [196]. The FI and second-rank CF parameters of fitting results are close to that at C_2 site in Y_2O_3:Eu^{3+}, but the other CF parameters differ appreciably in magnitude. Particularly, the $\mathrm{Im}B_4^4$, $\mathrm{Im}B_4^6$, $\mathrm{Im}B_6^6$ and $\mathrm{Re}B_6^6$ values of Eu^{3+} in In_2O_3 have opposite signs,

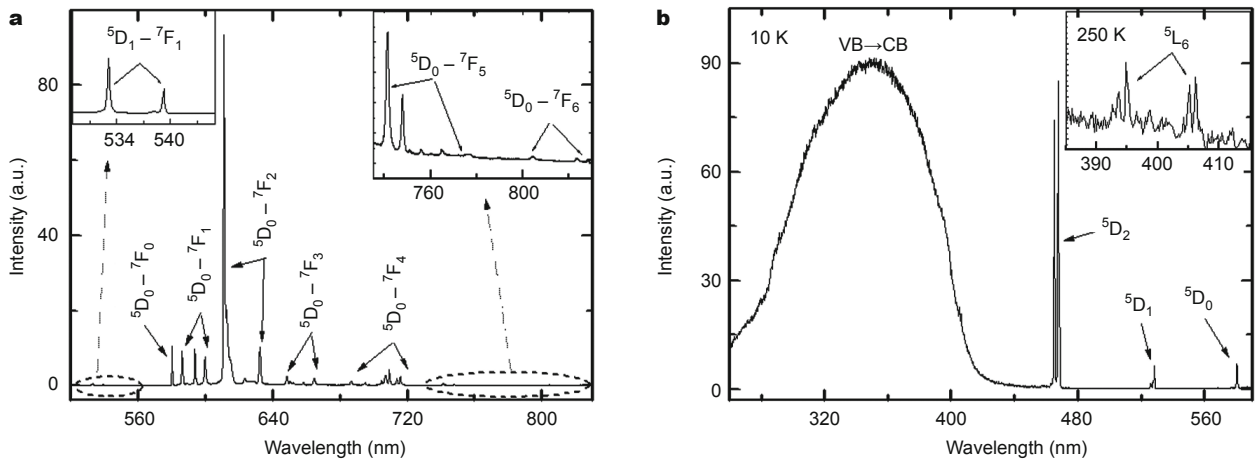

Figure 6 Optical spectra of Eu^{3+} at the C_2 site in In_2O_3 NCs. (a) 10 K emission spectrum upon excitation at 465.1 nm; (b) 10 K excitation spectra by monitoring the $^5D_0 \rightarrow {}^7F_2$ transition at 611.0 nm; the inset in (b) shows the 250 K excitation spectrum in the region of $^5L_6$. Reprinted with permission from Ref. [115]. Copyright 2010, American Chemical Society.

Table 6 Energy levels of Eu^{3+} at the C_2 site of In_2O_3 NCs (unit: cm^{-1}). Reprinted with permission from Ref. [115]. Copyright 2010, American Chemical Society

Multiplet	Energy		ΔE	Multiplet	Energy		ΔE
	Exp.	Fit			Exp.	Fit	
$^7F_0$	0	2	−2		–	5128	–
$^7F_1$	173	184	−11		–	5141	–
	389	396	−7		5159	5143	16
	566	582	−16		–	5405	–
$^7F_2$	866	852	14		–	5412	–
	900	879	21		–	5434	–
	975	961	14		–	5529	–
	1191	1172	19		–	5533	–
	1422	1415	7		–	5696	–
$^7F_3$	1797	1803	−6		–	5696	–
	1854	1867	−13	$^5D_0$	17,229	17,229	0
	1898	1908	−10	$^5D_1$	18,932	18,910	22
	1961	1963	−2		18,968	18,964	4
	2026	2037	−11		19,020	19,048	−28
	2176	2178	−2	$^5D_2$	21,365	21,372	−7
	–	2234	–		–	21,378	–
$^7F_4$	2663	2665	−2		21,395	21,392	3
	2812	2798	14		–	21,463	–
	2841	2851	−10		21,501	21,490	11
	3040	3039	1		–	24,153	–
	3085	3070	15		–	24,201	–
	3130	3128	2		–	24,227	–
	3219	3216	3		–	24,235	–
	3260	3252	8		–	24,261	–
	3283	3287	−4		–	24,282	–
$^7F_5$	3742	3739	3		–	24,291	–
	3856	3853	3	$^5L_6$	–	24,557	–
	3912	3903	9		–	24,595	–
	3933	3924	9		24,618	24,632	−14
	3999	3994	5		24,704	24,697	7
	4076	4078	−2		–	24,703	–
	–	4089	–		–	24,779	–
	4149	4157	−8		–	24,829	–
	4337	4342	−5		–	25,018	–
	4356	4358	−2		–	25,239	–
	–	4421	–		–	25,310	–
$^7F_6$	4798	4812	−14		25,329	25,330	−1
	–	4819	–		25,406	25,400	6
	5086	5104	−18		25,471	25,466	5

indicating a different CF environment experienced by Eu^{3+} in In_2O_3 host. The value of S for Eu^{3+} at the C_2 site of In_2O_3 was calculated to be 790 cm^{-1}.

Ln^{3+} doped Ga_2O_3 NCs

Gallium oxide (Ga_2O_3) has five crystal structures and β-Ga_2O_3 is the most stable phase, which is a semiconductor with a wide bandgap of ~4.8 eV [197,198]. The structure of β-Ga_2O_3 is monoclinic with a space group of $C_{2/m}$, and Ga^{3+} ions occupy two crystallographic sites, namely tetrahedral and octahedral, respectively [199]. β-Ga_2O_3 is a good host for Ln^{3+} ions due to its high thermal and chemical stability and wide range of optical transparency. To date, the visible to infrared luminescence of Ln^{3+} in Ga_2O_3 have been achieved under either photon or electron excitation [59,90,98,99,104,105,200–205]. However, the Ln^{3+} emission and excitation spectra previously reported show a broadband pattern rather than sharp transition lines that are typical of Ln^{3+} in a crystalline environment, indicating that Eu^{3+} ions might be located at the surface or close to the surface sites instead of entering the crystal lattice of β-Ga_2O_3. In our recent work, sharp emission lines of Eu^{3+} in β-Ga_2O_3 NCs prepared via a simple combustion method were observed (Fig. 7), suggesting that Eu^{3+} ions were embedded in β-Ga_2O_3 nano-lattice. Interestingly, it was observed that the substitution of Eu^{3+} for Ga^{3+} occurred at merely single site, in spite of two crystallographically non-equivalent sites of Ga^{3+} in β-Ga_2O_3. Spectroscopic evidence validated the local site symmetry of C_s for Eu^{3+} at this single site [83]. From the 10 K high-resolution excitation and emission spectra of Eu^{3+} in β-Ga_2O_3, 71 CF levels of Eu^{3+} were identified and listed in Table 7. The CF levels of Eu^{3+} were fitted at C_s symmetry using the *f*-shell empirical programs from Reid [185]. The detailed fitting procedure is similar to that in TiO_2:Er^{3+}. The FI parameters of LaF_3:Eu^{3+} [48] and CF parameters of Gd_2O_3:Eu^{3+} [182] were used as initial values in the fitting. The standard *rms* deviation of the final fit is 12.9 cm^{-1}, showing an excellent agreement between experimental and calculated values. The experimental and fitted CF levels below 34,000 cm^{-1} are compared in Table 7. The obtained FI and CF parameters are listed in Table 3. The calculated value of S is 546 cm^{-1} for β-Ga_2O_3:Eu^{3+}, which is much smaller than In_2O_3:Eu^{3+} (790 cm^{-1}) [115] with C_2 symmetry.

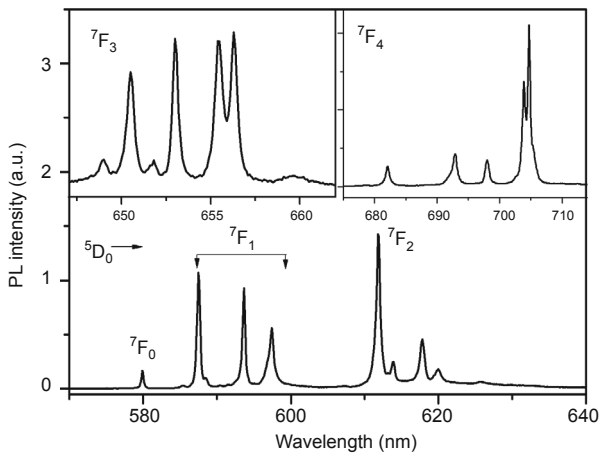

Figure 7 High-resolution PL spectra of Eu^{3+} in β-Ga_2O_3 NCs upon bandgap excitation at 10 K. Reproduced from Ref. [83] with permission from the PCCP Owner Societies.

DOPING LOCATION OF LANTHANIDE IONS IN SNCs

It is well known that the electronic structures of Ln^{3+} are closely related to their locations in the host materials [172]. Because of charge imbalance and lattice distortion, multiple sites of Ln^{3+} with distinct CF surroundings are prone to be formed by introducing Ln^{3+} ions into the lattices of SNCs. In view of the diverse CF surroundings, such multiple sites of Ln^{3+} are usually characterized by different PL patterns and decays, which will facilitate the survey of the local structures of Ln^{3+} ions in SNCs by means of the site-selective or time-resolved spectroscopic techniques.

Surface location of Ln^{3+} in SNCs

Due to the charge imbalance and the large discrepancy of ionic radius between Ln^{3+} and some of semiconductor cations, Ln^{3+} ions can hardly be incorporated into such kinds of SNCs lattice via common wet chemical method. Instead, in most cases, the dopant ions are prone to accumulate on the loosely-structured surface sites of the NCs. Because of the continuous distributions of Ln^{3+} in various surface sites, the luminescence spectra usually feature broad and unresolved bands.

As an example, the emission spectra of Eu^{3+} ions on the surface of TiO_2 and ZnO NCs are showcased in Fig. 8. For Eu^{3+} in both samples, the PL emission spectra exhibited broad bands originating from the $^5D_0$ to ^7F_J transitions, and the emission intensity of $^5D_0 \rightarrow {}^7F_2$ is much stronger than that of $^5D_0 \rightarrow {}^7F_1$, indicating that Eu^{3+} occupied in highly distorted non-centrosymmetric locations in the surface of SNCs. Thanks to the ease of the compensation for lattice distortion and charge imbalance on the surface, the maximal doping concentration of Ln^{3+} on the outer surface sites are usually much larger than that in the inner lattices of SNCs. As shown in Fig. 8a, the PL concentration quenching did not occur even when the Eu^{3+} concentration reached 16 mol.% in TiO_2 NCs. In addition to the Eu-re-

Table 7 CF levels of Eu^{3+} at the C_s site of β-Ga_2O_3 (unit: cm^{-1}). Reproduced from Ref. [83] with permission from the PCCP Owner Societies

Multiplet	Energy (cm^{-1})		Multiplet	Energy (cm^{-1})		Multiplet	Energy (cm^{-1})		Multiplet	Energy (cm^{-1})		Multiplet	Energy (cm^{-1})	
	Exp.	Fit		Exp.	Fit		Exp.	Fit		Exp.	Fit		Exp.	Fit
$^7F_0$	0	4		21,510	21,498		26,483	26,471		—	27,744		—	31,290
$^7F_1$	223	242		—	21,526		—	26,484		—	27,751		31,299	31,301
	401	402	$^5D_3$	24,284	24,273		—	26,495		—	27,834		—	31,313
	505	515		—	24,293		26,511	26,505		—	27,838		—	31,330
$^7F_2$	899	887		24,325	24,314		—	26,521		—	27,880		—	31,349
	955	943		—	24,335		—	26,529		—	27,883		—	31,355
	1058	1061		—	24,345		—	26,546		—	27,931		—	31,368
	1115	1103		—	24,356		—	26,548		—	27,964		31,377	31,389
	1265	1264		—	24,372		—	26,563		—	27,988		—	31,391
$^7F_3$	1836	1845	$^5L_6$	—	24,758		—	26,572		—	28,038		—	31,408
	1872	1858		—	24,772		—	26,573		—	28,044		—	31,421
	1902	1893		—	24,833		—	26,587		—	28,080		—	31,444
	1930	1933		24,876	24,878		26,617	26,612		—	28,087		—	31,469
	1986	1983		—	24,921		—	26,620		—	28,101		—	31,472
	2007	1990		24,963	24,934		—	26,668		—	28,107		—	31,473
	2086	2089		—	24,978		—	26,677		—	28,120		—	31,491
$^7F_4$	2584	2599		25,107	25,106		—	26,713		—	28,127		—	31,494
	—	2792		25,195	25,209		—	26,721		—	28,174		—	31,504
	2812	2814		25,253	25,257		—	26,724		—	28,186		—	31,539
	2918	2913		—	25,289		—	26,741		—	28,193		—	31,567
	—	2952		25,323	25,349		—	26,744		—	28,213		—	31,570
	3038	3033		25,400	25,370		—	26,745		—	28,317		—	31,570
	3054	3057	$^5G_{2,3}$	—	25,800		—	26,776		—	28,327		31,596	31,586
	—	3130	$^5G_{4,5}$	—	25,869		—	26,788		—	28,388		—	31,621
	—	3204	$^5G_6$	—	25,871		—	26,799		—	28,431		—	31,649
$^7F_5$	—	3741	$^5L_7$	—	25,892		26,817	26,805		—	28,455		31,676	31,679
	—	3745		25,900	25,893	$^5L_8$	—	26,933		—	28,541		—	31,690
	—	3881		—	25,927		—	26,949		—	28,566		—	31,696
	—	3957		25,947	25,947		—	26,972		—	28,575		—	31,722
	—	3991		25,974	25,970		—	26,974		—	28,594		—	31,731
	—	3994		25,994	26,000		27,020	27,033		—	28,680		—	31,761
	—	4024		—	26,035		—	27,054		—	28,696		—	31,792
	—	4106		—	26,055		—	27,089		—	28,778		—	31,809
	—	4147		—	26,078		—	27,094		—	28,778		—	31,834
	—	4203		26,123	26,118		—	27,166		—	28,791		—	31,834
	—	4271		—	26,150		—	27,188		—	28,793	$^3P_0$	—	32,366
$^7F_6$	—	4846		—	26,170		27,218	27,199	$^5H_{3,4}$	—	30,869	$^5F_{2,3}$	—	32,854
	—	4858		26,199	26,207		27,278	27,269	$^5H_{5,6}$	—	30,881		—	32,879
	—	4933		—	26,220		—	27,290	$^5H_7$	—	30,909		—	32,895
	—	4941		—	26,236		—	27,316		—	30,936		—	32,948
	—	5037		26247	26,242		27,322	27,332		—	30,949		32,960	32,954
	—	5060		—	26,258		—	27,337		—	30,959		—	32,967
	—	5221		26,288	26,281		—	27,349		30,979	30,962		33,014	33,015
	—	5235		—	26,295	$^5D_4$	—	27,472		—	30,978		—	33,031
	—	5286		—	26,295		—	27,499		—	31,034		—	33,050
	—	5316		—	26,349	$^5L_{9,10}$	27,533	27,528		—	31,037		33,102	33,104
	—	5327		—	26,355		—	27,548		31,075	31,075		—	33,162
	—	5462		—	26,359		—	27,564		—	31,099		—	33,194
	—	5463		—	26,367		—	27,574		—	31,131	$^5F_1$	—	33,324
$^5D_0$	17,244	17,232		26,385	26,397		27,586	27,590		—	31,162		—	33,343
$^5D_1$	18,975	18,959		—	26,402		—	27,609		—	31,186		—	33,356
	19,008	19,012		—	26,422		27,617	27,629		—	31,205	$^5F_4$	—	33,373
	19,033	19,053		—	26,434		27,647	27,643		—	31,213		—	33,397
$^5D_2$	21,436	21,445		—	26,436		—	27,644		—	31,229		—	33,402
	21,450	21,464		26,455	26,450		—	27,696		—	31,256		33,445	33,462
	21,468	21,478		—	26,468		27,693	27,702		—	31,285			

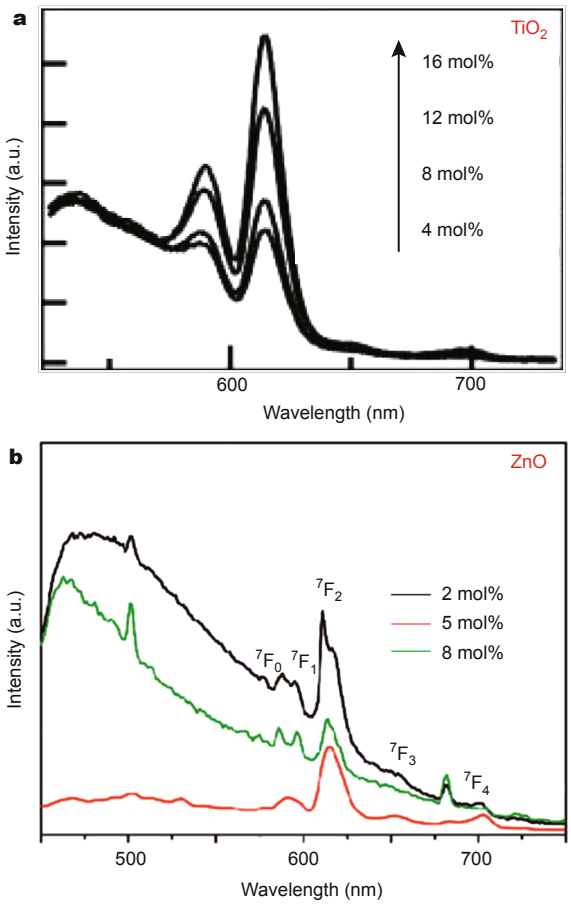

Figure 8 PL emission spectra of Eu^{3+} doped (a) TiO_2 (b) ZnO NCs upon excitation above the bandgap of TiO_2 (325 nm) and ZnO (380 nm), respectively. Adapted with permission from Refs. [37,38]. Copyright 2008, Wiley-VCH Verlag GmbH & Co. KGaA and American Chemical Society.

lated emission, the PL emission of surface defects typical of broad bands in the visible region was often observed to superpose on the emission spectra of Ln^{3+}. As shown in Fig. 8, the broad defect emission bands centered at around 525 nm were observed in both TiO_2 and ZnO samples. It should be noted that the energy transfer from the hosts to surface Ln^{3+} ions becomes easier with the aid of the surface defect states, as will be discussed later.

Multiple-site structure of Ln^{3+} ions

Site-selective spectroscopy

Due to the discrepancy of surroundings of Ln^{3+} ions in multiple sites of SNCs, both the PL emission and excitation spectra at each site usually exhibit distinctive optical characteristics in the line position and relative intensities. Site-selective spectroscopy is an effective technique to acquire the separated PL spectra of Ln^{3+} at multiple sites. To successfully separate the PL spectra of Ln^{3+} at each site, the primary condition is the insignificant spectral overlap between PL spectra of different sites at wavelengths selected as excitation or monitoring lines. Moreover, a low experimental temperature is commonly set to eliminate the influence of phonon broadening on the PL lines.

In our previous work, by using Eu^{3+} as a sensitive structural probe, we showed unambiguously the presence of multiple sites of Eu^{3+} in 9-nm hexagonal wurtzite ZnO NCs that were synthesized via a facile sol-gel method [59,206]. As compared in Fig. 9, two types of luminescence sites of Eu^{3+} were clearly identified by means of site-selective spectroscopy at low temperature (10 K). One site (denoted as

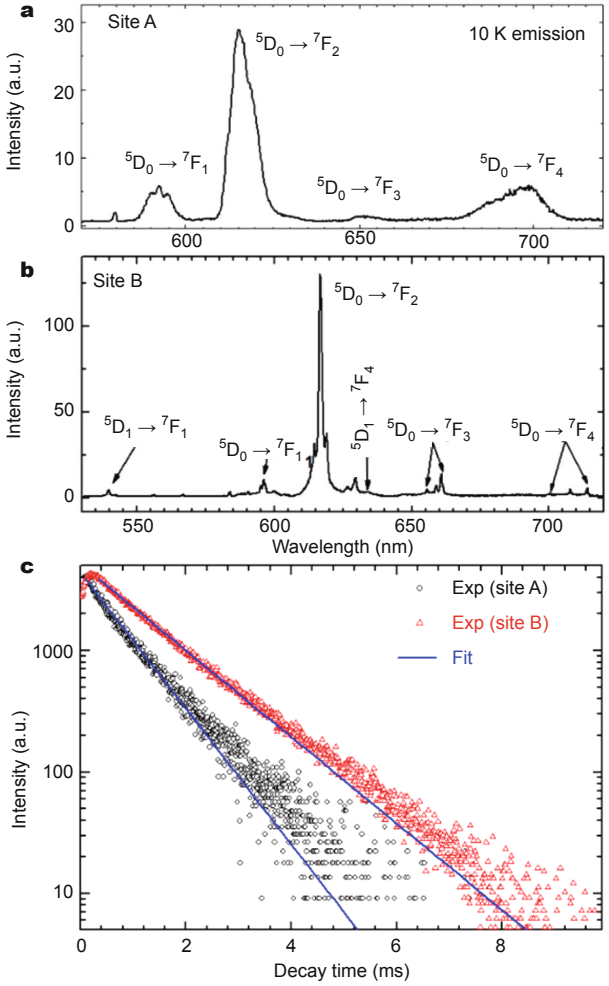

Figure 9 10 K site-selective PL emission spectra of ZnO:Eu^{3+} NCs under the (a) 465 nm excitation for Eu^{3+} at site A and (b) 467.8 nm excitation for Eu^{3+} at site B; (c) 10 K PL decays from $^5D_0$ of Eu^{3+} at sites A and B in ZnO:Eu^{3+} NCs under the site-selective excitation at 464.8 and 467.8 nm, respectively. Adapted with permission from Ref. [206]. Copyright 2007, Optical Society of America.

site A) exhibited broadened PL excitation and emission peaks with the most intense emission at 615 nm similar to that of Eu^{3+} ion in glasslike phase, which is associated with the distorted lattice sites near the surface. These broad emission lines centered at 580, 592, 615, 650 and 698 nm can be readily ascribed to the $^5D_0 \rightarrow ^7F_0$, $^5D_0 \rightarrow ^7F_1$, $^5D_0 \rightarrow ^7F_2$, $^5D_0 \rightarrow ^7F_3$, and $^5D_0 \rightarrow ^7F_4$ transitions of Eu^{3+}, respectively (Fig. 9a). Unlike site A, sharp PL excitation and emission lines of Eu^{3+} with the most intense emission lines at 616.6 nm were observed (Fig. 9b), which are originated from the Eu^{3+} ions located at a lattice site with ordered crystalline environment (denoted as site B). The value of full width at half-maximum height (FWHM) of site B is much smaller than that of site A, decreasing from ~8.0 nm (the 615-nm peak) to 0.9 nm (the 616.6-nm peak). In addition to these very sharp emission lines of the $^5D_0 \rightarrow ^7F_J$ (J=0,1,2,3,4) transitions, weak emission lines of the $^5D_1 \rightarrow ^7F_J$ (J=1,2,3,4) transitions of Eu^{3+} were also detected at 10 K (Fig. 9b), further revealing the much better crystalline surroundings for Eu^{3+} at site B relative to that at site A.

The PL lifetime (τ) depends significantly upon radiative and nonradiative decay rates of the excited state, which are bound up with the crystalline environment around the dopants [172]. Because of the existence of multiple sites of Ln^{3+} ions in SNCs, different luminescence decays of Ln^{3+} ions are expected in Ln^{3+} doped SNCs. For this reason, we detected two types of PL decays of Eu^{3+} in ZnO:Eu^{3+} NCs when monitoring the site-selective emissions of Eu^{3+} at the surface and lattice sites (Fig. 9c) [59]. For Eu^{3+} at the surface site (site A), the PL decay exhibits a single exponential behavior, and the $^5D_0$ lifetime was determined to be 0.75 ms by fitting with single exponential function. Unlike Eu^{3+} ions at site A, the PL decay from $^5D_0$ of Eu^{3+} at the lattice site (site B) features a noticeable rising edge at the initial stage and a single exponential decay in the tail when excited to the $^5D_2$ state. The intrinsic lifetime of $^5D_0$ was estimated to be 1.25 ms from the tail at 10 K. Moreover, the luminescence lifetime of $^5D_0$ of Eu^{3+} in ZnO NCs was observed to be weakly dependent on the temperature due to the large energy gap between $^5D_0$ and its next low-lying $^7F_6$ (~12,000 cm^{-1}). The $^5D_0$ lifetime of sites A and B were determined to be 0.69 and 1.05 ms by monitoring the site-selective emission ($^5D_0 \rightarrow ^7F_2$) at room temperature, respectively.

Another typical example for multiple-site structures of Eu^{3+} was exemplified in anatase TiO_2 aggregates assembled from the 10–12 nm TiO_2 NCs (Fig. 10a) [178]. As illustrated in Fig. 10, the PL excitation and emission patterns of Eu^{3+} ions at three sites differ obviously from each other in line positions, shapes and intensities, indicative of a totally different CF environment experienced by Eu^{3+} ions in TiO_2:Eu^{3+} NCs. When excited at 464.6 nm, the TiO_2:Eu^{3+} NCs exhibit broadened emission lines with the most intense peak centered at 613.3 nm similar to that of Eu^{3+} in glasslike phase (Fig. 10b), which is ascribed to the distorted lattice site near the surface (marked as site I). In stark contrast, upon selective excitations at 470.7 and 472.1 nm, much sharper emission lines with the most intense peaks at 616.7 and 618.1 nm are observed relative to that of site I (Figs 10c and d), which are originated from the lattice sites with ordered crystalline environment in anatase TiO_2 (marked as sites II and III, respectively). It should be noted that, due to the spectral overlap between the monitored

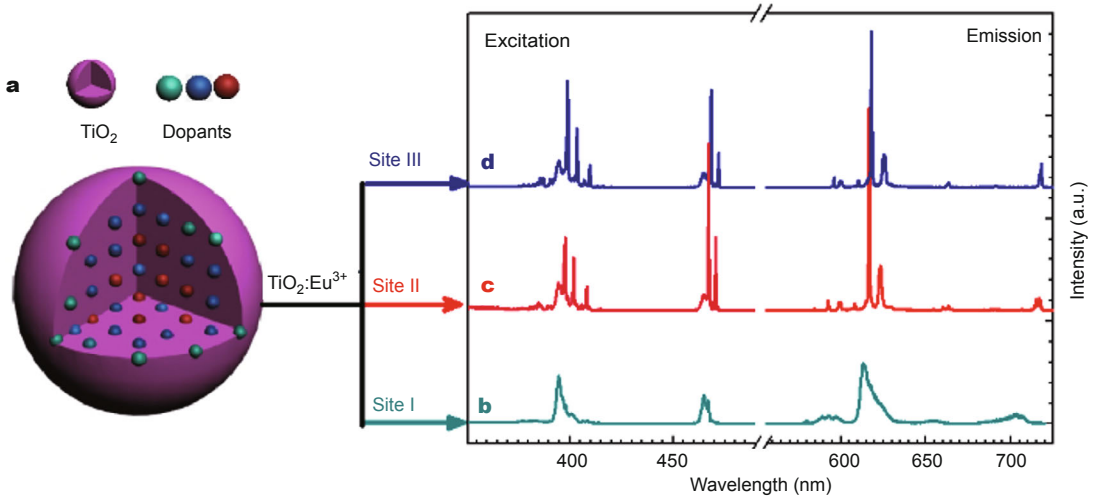

Figure 10 (a) A schematic illustration showing Eu^{3+} ions doped TiO_2 NCs with multiple luminescence centers of Eu^{3+}; 10 K excitation spectra (left) of TiO_2:Eu^{3+} NCs annealed at 400°C by monitoring the $^5D_0 \rightarrow ^7F_2$ emissions at (b) 613.3 nm, (c) 616.7 nm, and (d) 618.1 nm for sites I, II and III, respectively; and 10 K emission spectra (right) of TiO_2:Eu^{3+} annealed at 400°C, with (b) λ_{ex} = 464.6 nm for site I, (c) λ_{em} = 470.7 nm for site II, and (d) λ_{ex} = 472.1 nm for site III. Adapted with permission from Ref. [178]. Copyright 2008, American Chemical Society.

emission lines at 616.7 nm for site II (or at 618.1 nm for site III) and broad emission at 613 nm for site I, the excitation lines of site I were found to mingle into the site-selective excitation spectra of site II and III.

Time-resolved PL spectroscopy

In addition to the site-selective spectroscopy aforementioned, time-resolved PL (TRPL) technique is another useful means to identify multiple Ln^{3+} sites in SNCs. For example, we were unable to pick out the PL from single Nd^{3+} site by the site-selective spectroscopy, owing to the very close CF levels (~13 cm^{-1}) of $^4F_{3/2}$ for various Nd^{3+} ions in ZnO NCs [207]. As shown in Fig. 11a, upon direct excitation from the ground state $^4I_{9/2}$ to the $^4F_{5/2}$ state of Nd^{3+} at 811 nm, three broad emission bands centered at 898, 1082 and 1373 nm can be observed at room temperature, which are attributed to the radiative relaxations from $^4F_{3/2}$ to its low-lying multiplets of $^4I_{9/2}$, $^4I_{11/2}$ and $^4I_{13/2}$, respectively. Meanwhile, much sharper and better resolved emission lines originating from CF levels of $^4F_{3/2}$ to that of $^4I_{9/2}$, $^4I_{11/2}$ and $^4I_{13/2}$ were also detected at low temperature (4.2 K) (Fig. 11b). Owing to the time-reversal (Kramers) degeneracy for the $4f^3$ configuration (Nd^{3+}), theoretically, five emission peaks for the transition from $^4F_{3/2}$ to $^4I_{9/2}$ are expected for single Nd^{3+} site in ZnO NCs at 4.2 K. However, as depicted in the inset of Fig. 11b, ten moderately resolved transition lines assigned to $^4F_{3/2}$→$^4I_{9/2}$ were identified upon direct excitation at 811 nm, which thus corroborated that the emission lines in Fig. 11b derived from the PL superimposition of at least two Nd^{3+} sites in ZnO lattices.

As opposed to the high-resolution site-selective spectra in Fig. 11b, such multiple Nd^{3+} sites in ZnO NCs were easily distinguishable from each other in the time domain despite of the low spectral resolution (10 nm) in the frequency domain. Fig. 11c shows the TRPL spectra of ZnO:Nd^{3+} NCs collected at different delay time ranging from 0 to 85 μs. The intensity of emission peak centered at 1066 nm (peak A) was observed to increase dramatically with increasing delay time, reaching the maximum at ~10 μs, and then became undetectable after a delay time of ~30 μs. Nevertheless, a much slower time evolution process was observed for emission peak at 1082 nm (peak B). This noticeable difference in the evolution of peaks A and B was mainly caused by the multiple luminescence centers of Nd^{3+} ions in the lattice sites of ZnO NCs that possess various CF surroundings and therefore different decay behaviors [207].

Single lattice site of Ln^{3+} ions

Distinct from that observed in Eu^{3+} ions doped TiO_2 NCs, only one single lattice site of Er^{3+} was observed in anatase TiO_2:Er^{3+} NCs, which was unusual in view of the large mismatch of ionic radius and charge imbalance between Er^{3+} and Ti^{4+} [136]. To probe the CF surroundings experienced by Er^{3+} ions in TiO_2 NCs, the NIR PL spectra of Er^{3+} were measured upon bandgap excitation at 358 nm and direct excitation at 523.4 nm. As shown in Fig. 12a, almost the same NIR PL pattern attributed to the $^4I_{13/2}$→$^4I_{15/2}$ transition of Er^{3+} was detected despite the different excitation paths, which thereby revealed the single lattice site for the doped Er^{3+} ions in TiO_2 NCs. Fig. 12b exhibits the 10 K excitation spectrum for Er^{3+} doped TiO_2 NCs when monitoring the NIR $^4I_{13/2}$→$^4I_{15/2}$ emission at 1532.6 nm. Abundant sharp excitation lines of Er^{3+} centered at 380.6, 407.6, 489.4, 523.4, 550.5, and 654.0 nm can be detected, which come from

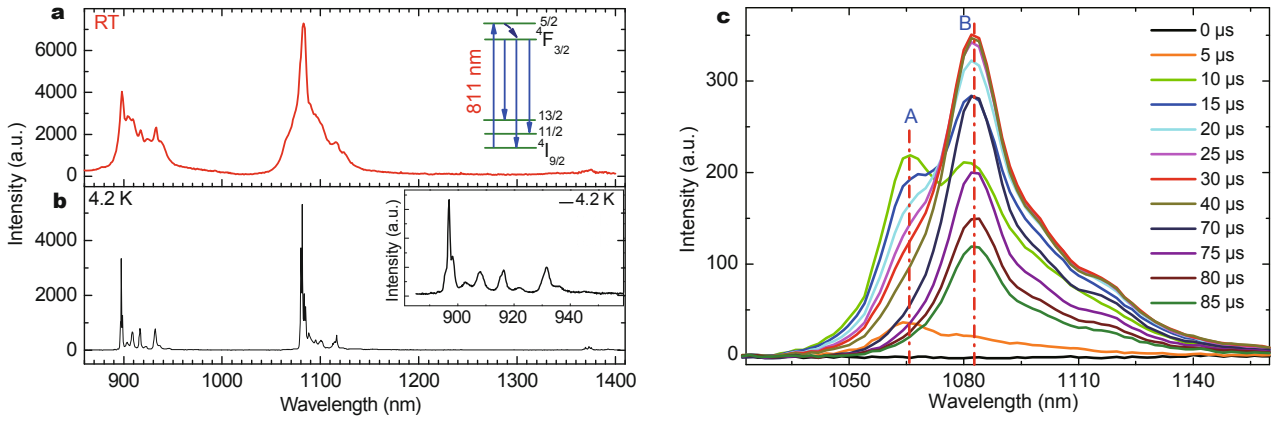

Figure 11 Room-temperature (a) and 4.2 K (b) NIR luminescence of Nd^{3+} ions doped ZnO NCs (the insets show the schematic diagram of excitation and emission levels of Nd^{3+} and the enlarged 4.2 K emission lines in the spectral region from 890 to 950 nm), and (c) TRPL spectra of Nd^{3+} ions in ZnO NCs. All the spectra were measured under the laser excitation at 811 nm. Adapted with permission from Ref. [207]. Copyright 2009, Optical Society of America.

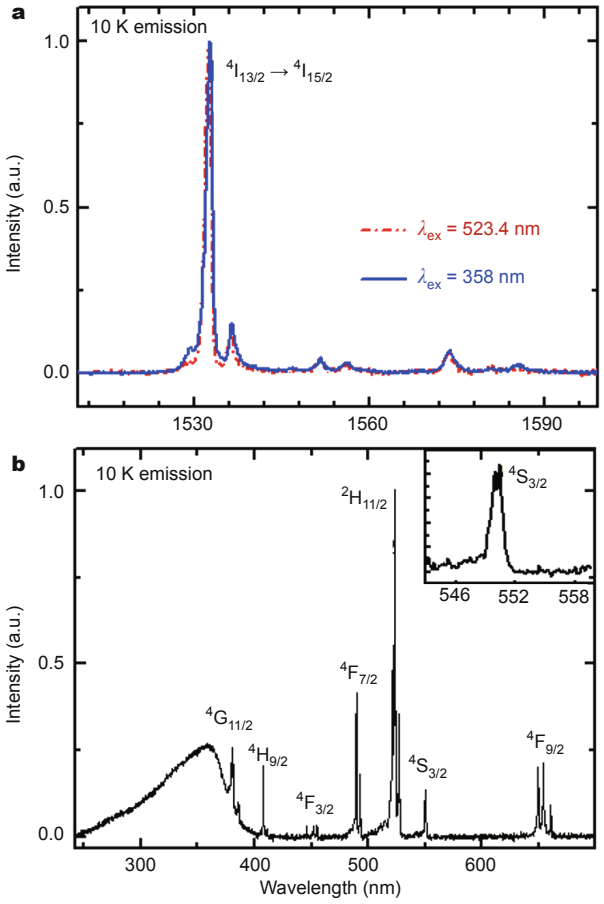

Figure 12 (a) 10 K NIR PL spectra for TiO_2:Er^{3+} NCs when directly and indirectly excited at 523.4 and 358 nm, respectively; and (b) 10 K PL excitation spectrum of TiO_2:Er^{3+} NCs (the inset enlarged the excitation lines for the transition of $^4I_{15/2} \rightarrow {}^4S_{3/2}$). Adapted with permission from Ref. [136], Copyright 2008, Optical Society of America.

the direct excitation from the ground state of $^4I_{15/2}$ to the upper excited states of $^4G_{11/2}$, $^2H_{9/2}$, $^4F_{7/2}$, $^2H_{11/2}$, $^4S_{3/2}$ and $^4F_{9/2}$, respectively. Fine CF splitting of the excited states of Er^{3+} is distinguishable, suggesting that Er^{3+} ions are situated at a lattice site rather than on the surface of TiO_2 NCs.

According to the crystal structure of anatase TiO_2, Er^{3+} ions occupying the Ti-lattice site should possess a D_{2d} site symmetry. Nevertheless, the actual site symmetry of Er^{3+} in TiO_2 lattice site may be reduced from D_{2d} to lower symmetries due to the remarkable lattice distortion induced by the significant difference in chemical properties for Ti^{4+} and Er^{3+} ions. Theoretically, the multiplets of Er^{3+} at D_{2d} or lower symmetry sites should present J+1/2 lines due to the Kramers degeneracy of $4f^{11}$ configuration for Er^{3+}. As clearly presented in the inset of Fig. 12b, only two excitation lines assigned to the excited state of $^4S_{3/2}$ and no trace of CF splitting due to another site can be detected. The CF splittings of other excited states in Fig. 12b also agree well with the theoretical analysis, further verifying the single lattice site of Er^{3+} ions in TiO_2 NCs. Based on these spectroscopic evidence, we infer that most of Er^{3+} ions are very likely located at the substitutional Ti^{4+} lattice site with a site symmetry descending from D_{2d} to C_{2v}, as revealed in Eu^{3+} doped TiO_2 NCs [178].

Similarly, such single lattice site of Er^{3+} was observed in Er^{3+} doped SnO_2 NCs. By using a solvothermal approach followed by annealing in oxygen atmosphere at 800–1100°C, Er^{3+} ions were successfully incorporated into the lattices of rutile SnO_2 NCs, which gave rise to typical NIR 1.54 μm emissions of Er^{3+} upon excitation above the SnO_2 bandgap at 300 nm [69]. As shown in Fig. 13a, the PL excitation spectrum of Er^{3+} in SnO_2 NCs is dominated by a strong UV broadband centered at ~300 nm that corresponds to the bandgap absorption peak of SnO_2 NCs (Fig. 13a, left), while the emission spectrum displays the fingerprint of Er^{3+} ions (Fig. 13a, right) when indirectly excited at ~300 nm, verifying the occurrence of energy transfer from SnO_2 NCs to emitters (Er^{3+}). These sharp and well-resolved NIR emission lines centered at ~1551 nm are attributed to the $^4I_{13/2} \rightarrow {}^4I_{15/2}$ transition of Er^{3+} in the lattices of rutile SnO_2 NCs. More importantly, it was found that these emission lines of Er^{3+} kept unchanged in terms of line positions and splittings for the samples annealed at temperatures of 800–1100°C, indicating the identical site occupation of Er^{3+} in SnO_2 NCs. Most likely, Er^{3+} ions were located at a lattice site with D_{2h} centrosymmetric site symmetry after the replacement for Sn^{4+} in SnO_2 NCs. This hypothesis was consistently supported by the absence of direct 4f-4f excitation lines of Er^{3+} in the PL excitation spectrum (Fig. 13a, left). According to the selection rule for the 4f-4f transitions of Ln^{3+} ions, electric-dipole (ED) transitions are strictly forbidden for a site with a center of inversion. As a consequence, the direct 4f-4f excitation lines, which correspond to the transitions from the ground multiplet $^4I_{15/2}$ to the excited states of Er^{3+} in the visible and NIR spectral regions (380~1000 nm), are forbidden due to their ED nature. To further identify the emission lines in Fig. 13a, high-resolution temperature-dependent emission spectra were measured from 10 to 300 K based on the Boltzmann distribution nature of electrons in those sublevels of $^4I_{13/2}$ and $^4I_{15/2}$. As recorded in Figs 13b and c, all emission lines can be well assigned and total 20 energy levels including 4 $^4I_{13/2}$ sublevels and 5 $^4I_{15/2}$ sublevels can be identified according to the variation of the emission line intensity with the change of experimental temperatures, further confirming the single lattice site occupation of Er^{3+} in SnO_2 NCs.

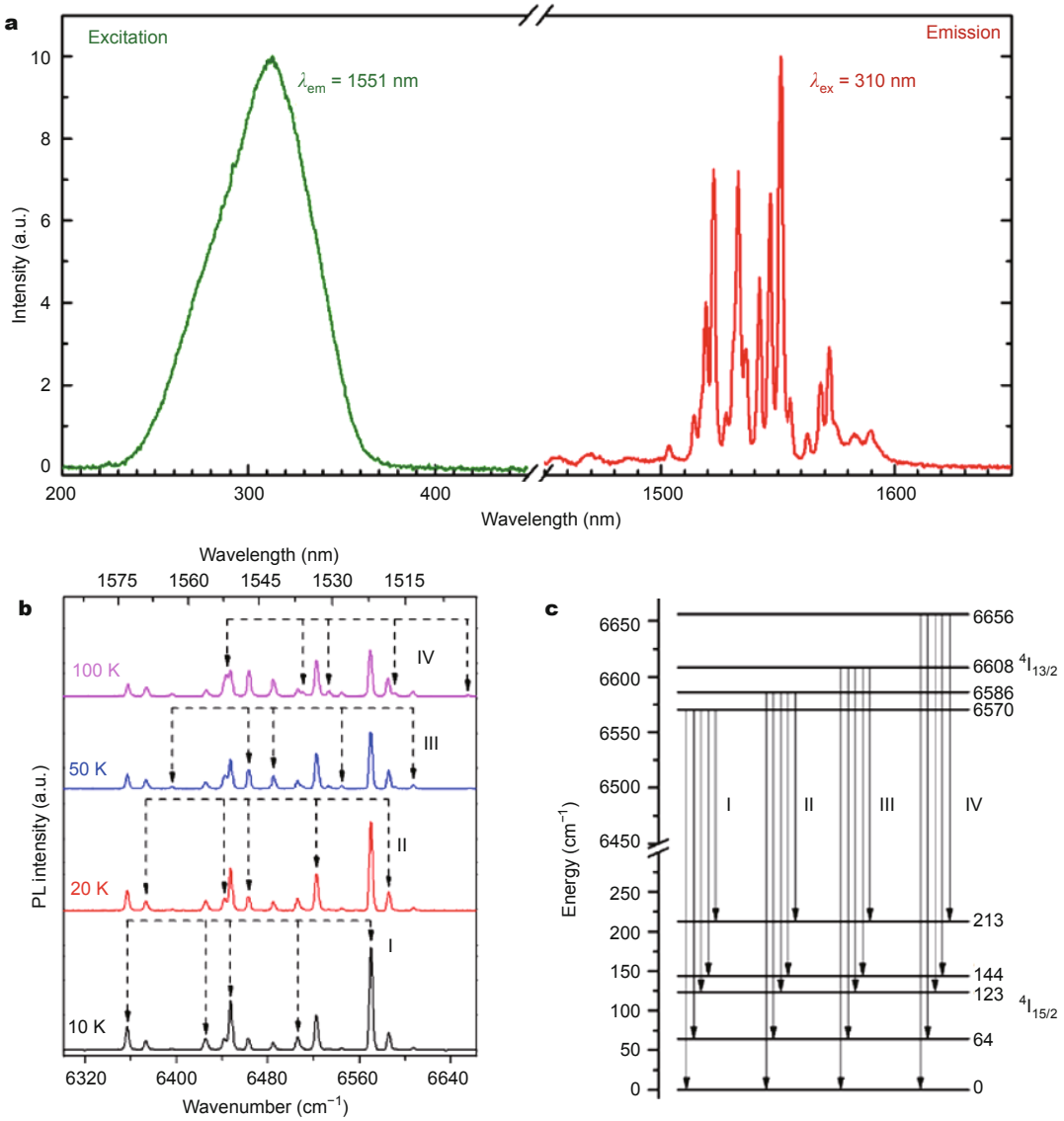

Figure 13 (a) PL excitation and emission spectra for SnO_2:Er^{3+} NCs at room temperature. (b) High-resolution emission spectra at 10, 20, 50, and 100 K upon excitation at 300 nm. (c) Illustration on energy levels and the transition from $^4I_{13/2}$ to $^4I_{15/2}$. I, II, III, and IV represent the transitions from the lowest four sublevels of $^4I_{13/2}$ to the sublevels of $^4I_{15/2}$, respectively. Adapted with permission from Ref. [69]. Copyright 2009, Optical Society of America.

HOST SENSITIZED LUMINESCENCE

Host sensitization via the energy transfer from the excited semiconductor host to Ln^{3+} is considered to be an effective way to realize highly efficient luminescence of Ln^{3+} for practical applications such as optoelectronic devices and flat panel displays [51,127,187]. In general, energy transfer involves the nonradiative energy transfer from a donor (sensitizer) to an acceptor separated in a solid by distances greater than the inter-atomic separations. The transfer is resonant if the energy matches the difference in electronic energy between levels of both the donor and acceptor systems. More often, nonresonant energy transfer involves the creation of phonons at the donor and/or acceptor sites. In case of Ln^{3+} doped semiconductor crystals, the energy transfer proceeds via a quite different way, i.e., via exciton recombination. As illustrated in Fig. 14a, by absorption of an excitation photon, the electron in the valence band (VB) is excited into the conduction band (CB) with a hole left in the VB. The electron and positively charged hole form an exciton pair, which can transport through the crystal lattice. Such an exciton pair can be trapped at defect sites in the lattice such as Ln^{3+} substitution. Followed by exciton

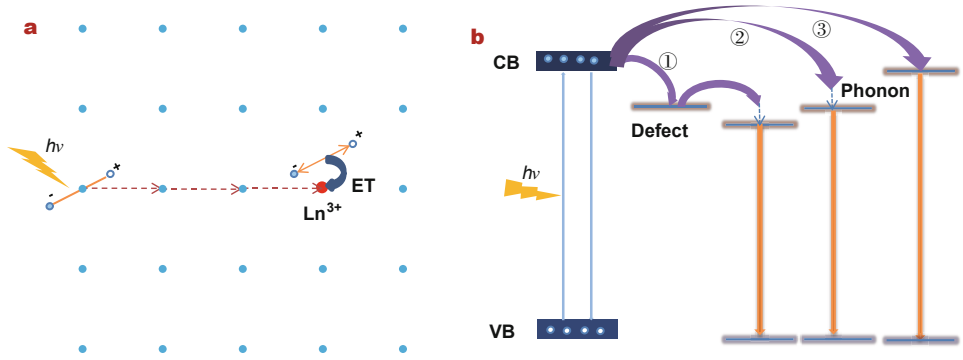

Figure 14 Proposed energy transfer (ET) mechanism in Ln^{3+} doped SNCs.

recombination, if spectrally matched, the energy can be transferred from the SNC host to Ln^{3+}.

It's worthy of mentioning that, to achieve efficient energy transfer from host to dopant, the excited-state levels of Ln^{3+} should be equal (resonant condition) or slightly lower (nonresonant condition) than the bandgap energy of SNCs. In the latter, the energy transfer occurs via phonon assistance or defect mediated way, which is commonly observed in Ln^{3+} doped SNCs (Fig. 14b). For instance, efficient energy transfer is observed in Nd^{3+} or Sm^{3+} doped TiO_2 NCs due to the small energy discrepancy between TiO_2 bandgap and excited states of Nd^{3+} or Sm^{3+} [187]. Fig. 15 shows the room-temperature excitation and emission spectra of Nd^{3+} and Sm^{3+} ions embedded in anatase TiO_2 NCs synthesized via a facile sol-gel solvothermal method [187]. Intense NIR PL of Nd^{3+} is observed upon excitation above the TiO_2 bandgap at 345 nm. Typical emission lines of Nd^{3+} centered at 915, 1094 and 1384 nm are explicitly assigned to the transitions from $^4F_{3/2}$ to $^4I_{9/2}$, $^4I_{11/2}$ and $^4I_{13/2}$, respectively (Fig. 15b). Meanwhile, sharp emission lines from Sm^{3+} in the region of 560–750 nm are also observed when excited with the same excitation light. The emission lines centered at 584.1, 612.8, 664.1 and 727.0 nm are attributed to the de-excitation from $^4G_{5/2}$ to its lower multiplets of $^6H_{5/2}$, $^6H_{7/2}$, $^6H_{9/2}$ and $^6H_{11/2}$ of Sm^{3+}, respectively (Fig. 15c). Taken together, these results strongly imply that the Nd^{3+} and Sm^{3+} emissions can be achieved via an efficient nonradiative energy transfer process from TiO_2 to the dopants, which is further evidenced by the presence of the intense bandgap absorption peak of anatase TiO_2 in the excitation spectra of TiO_2:Nd^{3+} and TiO_2:Sm^{3+} NCs (Fig. 15a). Moreover, it should be noted that the excitation lines arising from 4f-4f transitions of Nd^{3+} (or Sm^{3+}) itself in the room-temperature excitation spectrum were hardly detectable, thus revealing that the sensitized emission was a much more efficient pathway than the direct excitation of

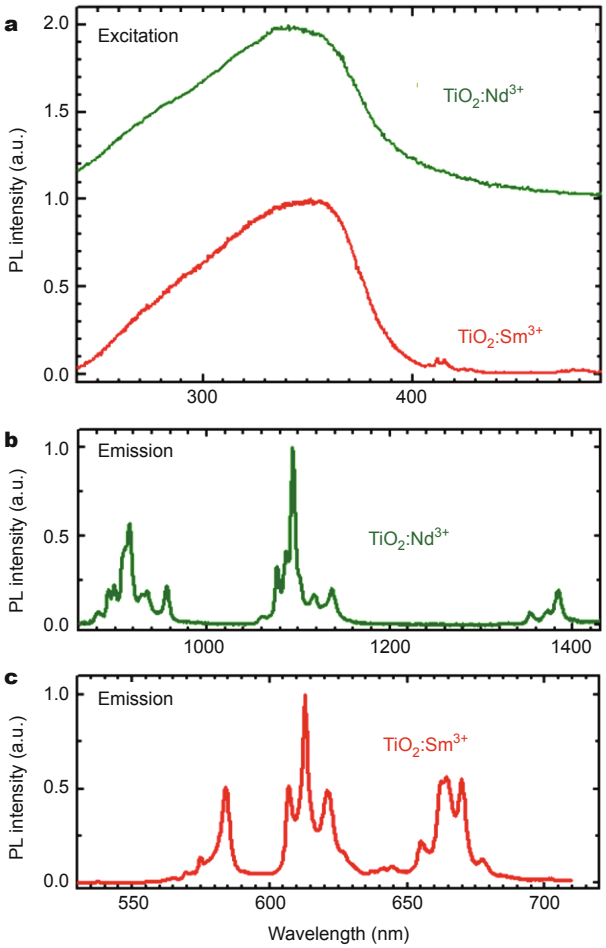

Figure 15 PL excitation (a) and emission (b, c) spectra for TiO_2:Nd^{3+} and TiO_2:Sm^{3+} NCs at room temperature, Adapted with permission from Ref. [187]. Copyright 2009, American Chemical Society.

Nd^{3+} or Sm^{3+} ions.

Unlike Nd^{3+} (or Sm^{3+}) doped TiO_2 NCs, TiO_2:Eu^{3+} NCs prepared by similar method exhibited only weak energy

transfer from TiO_2 host to Eu^{3+} ions at low temperature (10 K) due to the mismatch of energy between the TiO_2 bandgap and Eu^{3+} excited states [178]. To bridge the energy gap between the TiO_2 and Eu^{3+} excited states, a feasible alternative way is co-doping another Ln^{3+} ion as a mediated level. Ln^{3+} ions with rich ladder-like electronic structures prove to be effective energy bridges in tailoring the light output of phosphors. For this purpose, Sm^{3+} was introduced as an energy bridge, taking into account the fact that efficient energy transfer from the TiO_2 to Sm^{3+} [187] and the $^4G_{5/2}$ state of Sm^{3+} to the $^5D_0$ state of Eu^{3+} [210] were achieved. As expected, the energy transfer efficiency from TiO_2 to Eu^{3+} was greatly enhanced by co-doping 0.5 at.% Sm^{3+} ions into TiO_2:Eu^{3+} NCs [208]. Fig. 16a compares the excitation spectra of Eu^{3+} singly doped and Sm^{3+}/Eu^{3+} co-doped TiO_2 NCs by monitoring the $^5D_0 \rightarrow {}^7F_2$ transition of Eu^{3+} at 617.8 nm. Sharp emission lines centered at 394, 468.2, and 539.4 nm, which correspond to intra-4f transitions from $^7F_0$ ground state to the excitation multiplets of $^5L_6$, $^5D_2$, and $^5D_1$, dominated the excitation spectrum of Eu^{3+} singly doped TiO_2 NCs. In stark contrast, a broad band centered at 330 nm due to the TiO_2 bandgap absorption emerged in the excitation spectrum of Sm^{3+}/Eu^{3+} co-doped counterparts, indicating the existence of efficient energy transfer from the TiO_2 host to the Eu^{3+} ions with the aid of Sm^{3+} ions. The underlying energy transfer mechanism was schematically illustrated in Fig. 16b. The energy absorbed by TiO_2 host was first nonradiatively transferred to the excited state of Sm^{3+}, followed by the nonradiative relaxation to the long-lived $^4G_{5/2}$ of Sm^{3+}. The excited Sm^{3+} ions can then partially transfer their energy from $^4G_{5/2}$ to the $^5D_0$ level of $Eu^{3+}$and resulted in the intense red emission of Eu^{3+}.

Another strategy for the energy bridge in the host-to-Ln^{3+} energy transfer process is through defect states in NCs. In Ln^{3+} doped SNC systems, various defects are often generated as a result of lattice distortion and/or charge compensation due to the substitution of host cations with larger Ln^{3+} ions. Particularly, in nanomaterials, large specific surface area results in plenty of diverse surface defects. All these defects may play important roles in the optical performance of Ln^{3+} doped SNCs, for instance, being luminescent quenching centers, activators or energy transfer bridges.

In a nonresonant energy transfer process, phonons play a key role in bridging the energy mismatch between the bandgap of SNCs and the excited state of Ln^{3+}. However, the energy transfer efficiency decreases gradually with the increase of the number of phonons involved in the energy transfer process when the phonons are more than five. To this end, an effective way to assist the nonresonant energy transfer process is using defects as intermediate states. Such defect-mediated energy transfer from SNCs to Ln^{3+} ions was documented in the literature [49,127]. In particular, Wang and co-workers [209] demonstrated a defect-mediated energy transfer pathway from the ZnO host to the Eu^{3+} ions evidenced by temperature-dependent and time-resolved PL experiments. Upon excitation above the ZnO bandgap at 325 nm, emission lines at 375, 520 and 615 nm,

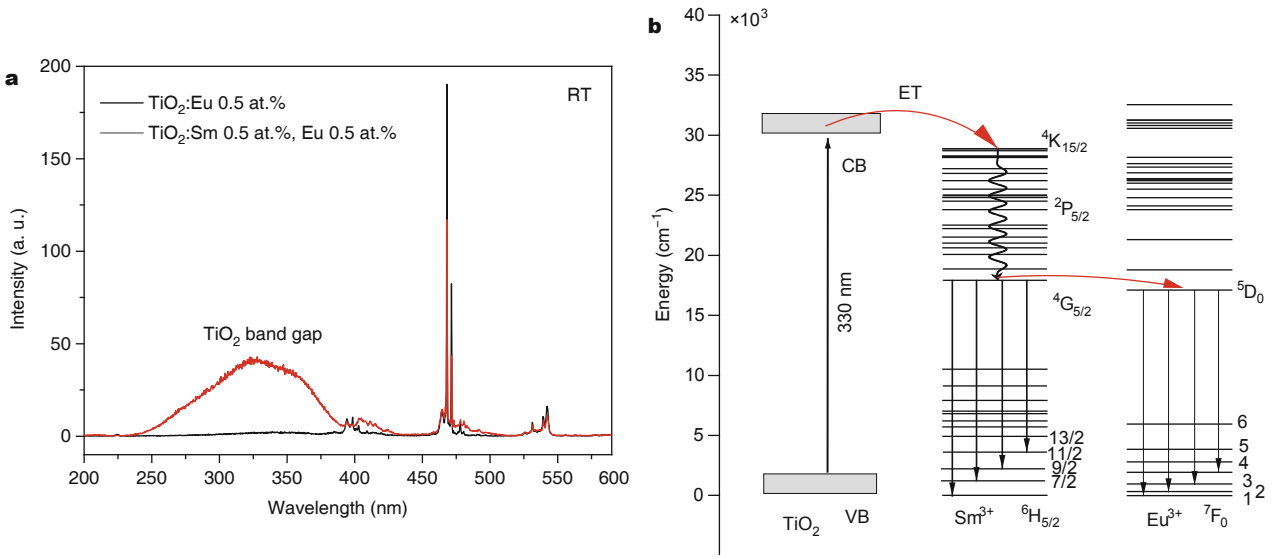

Figure 16 (a) Room-temperature excitation spectra of TiO_2:Sm^{3+} (0.5 at.%), Eu^{3+} (0.5 at.%) and TiO_2:Eu^{3+} (0.5 at.%) NCs by monitoring the $^5D_0 \rightarrow {}^7F_2$ emission of Eu^{3+} ions at 617.8 nm. (b) A schematic illustration of the energy transfer mechanism from the TiO_2 bandgap to Sm^{3+} and Eu^{3+} ions. Adapted with permission from Ref. [208]. Copyright 2010, American Scientific Publishers.

which are ascribed to the near-band edge (NBE) exciton recombination, defect states (oxygen vacancies) luminescence (DSL), and the $^5D_0 \rightarrow {}^7F_2$ transition of Eu^{3+} were found to dominate the emission spectra at different temperatures ranging from 5 to 300 K, indicating an energy transfer process from the host to Eu^{3+}. Moreover, temperature-dependent Eu^{3+} emission exhibited similar features to that of defect related emission, suggesting that the defect state may act as an energy reservoir in mediating the energy transfer from ZnO host to Eu^{3+} (Fig. 17a). To further establish this relationship, the PL emission spectra and excited state dynamics of the as-prepared sample (EZO-1) and the counterpart annealed at 600°C in air (EZO-2) were compared in Figs 17b and c. Note that the content of oxygen vacancies in EZO-2 was remarkably reduced after annealing. Consistently, with the decrease of defects in the sample (namely, a decrease of oxygen deficiency from ~26% in EZO-1 to ~8.4% in EZO-2), the Eu^{3+} related emission decreased, thus confirming that oxygen vacancy defects acted as the intermediate state in the energy transfer process (Fig. 17d).

Another interesting example of defect mediated energy transfer was reported by Tachikawa *et al.* [166], who employed single-molecule (single-particle) fluorescence spectroscopy to investigate the PL dynamics of Eu^{3+} doped TiO_2 NCs. During the PL measurements upon 405-nm laser excitation, the concentration of defects (oxygen vacancies) in TiO_2 nanoparticles could be tuned by altering the experimental atmosphere, which enables the *in situ* exploration of the impact of defects on the PL properties of TiO_2:Eu^{3+} nanoparticles at single particle level. As demonstrated in Fig. 18a, with the stimulation at 405-nm laser in Ar atmosphere which resulted in the increase of light induced surface defects in TiO_2 nanoparticles, the brightness of PL containing both the defect-related and Eu^{3+} emissions increased dramatically. Moreover, it was found that the PL bands in the region of 500–750 nm relative to surface defect emission appeared and increased with the continuous 405-nm laser stimulation in Ar atmosphere (Figs 18b and d). Meanwhile, the PL intensity of $^5D_0 \rightarrow {}^7F_1$ (590 nm) increased with increasing irradiation time, whereas the

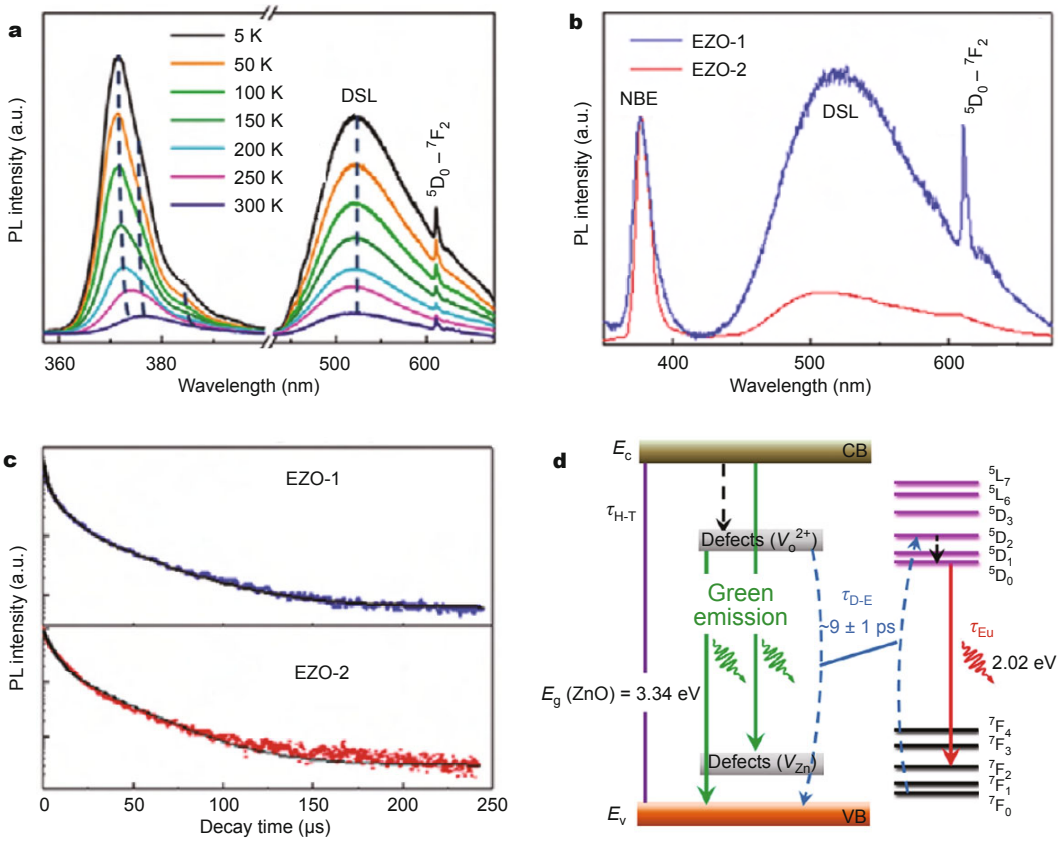

Figure 17 (a) Temperature-dependent PL spectra of as-prepared Eu^{3+} doped ZnO nanowires (EZO-1) upon excitation at 325 nm; (b) room-temperature emission spectra of EZO-1 and the annealed sample (EZO-2) upon excitation at 325 nm. (c) PL decays of Eu^{3+} in EZO-1 and EZO-2 by monitoring the 615 nm emission upon excitation at 325 nm. (d) A schematic illustration of the proposed mechanism of energy transfer from the ZnO host to the Eu^{3+} ions. Adapted with permission from Ref. [209]. Copyright 2011, American Chemical Society.

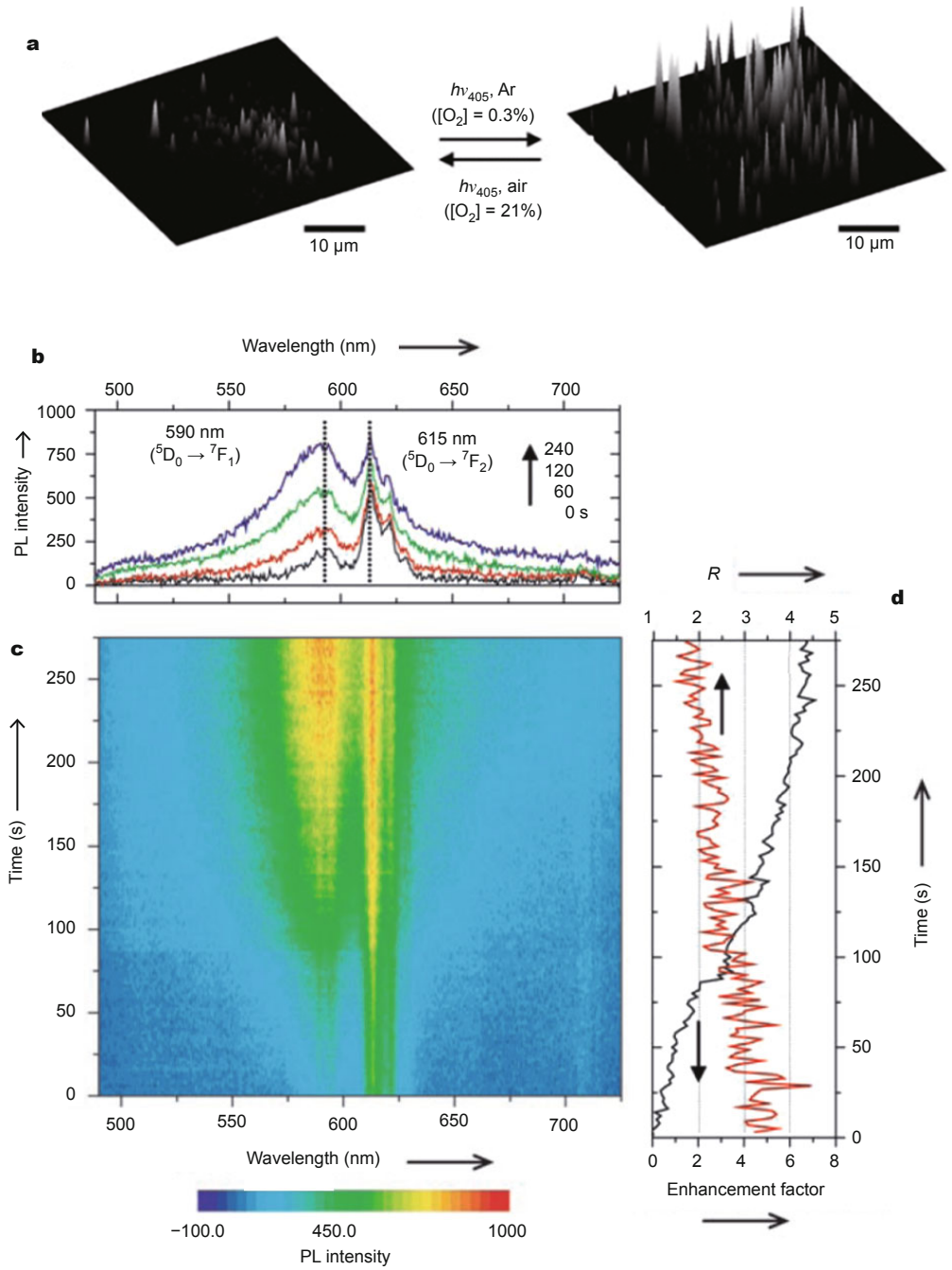

Figure 18 (a) Typical emission spots of TiO_2:Eu^{3+} nanoparticles (or aggregates) upon 405-nm laser excitation in air (left) or Ar (right) atmospheres. Time evolutions of the PL spectra (b) and image (c) upon excitation for a single TiO_2:Eu^{3+} nanoparticle (or aggregate) in Ar atmosphere. d) The dependence of the PL intensity enhancement factor at 550 nm (the ratio of the differential PL intensity to the original intensity) and *R* value (PL intensity ratio of $^5D_0 \rightarrow {}^7F_2$ to $^5D_0 \rightarrow {}^7F_1$) on the 405-nm laser irradiation times. Adapted with permission from Ref. [166]. Copyright 2008, Wiley-VCH Verlag GmbH & Co. KGaA.

PL intensity of $^5D_0 \rightarrow {}^7F_2$ (615 nm) followed opposite trend. The $^5D_0 \rightarrow {}^7F_2$ transition is of forced ED nature and ultrasensitive to the local environment of Eu^{3+} ions, while the magnetic-dipole (MD) allowed $^5D_0 \rightarrow {}^7F_1$ is essentially not influenced. The relative PL intensity ratio (*R*) of $^5D_0 \rightarrow {}^7F_2$ (615 nm) to $^5D_0 \rightarrow {}^7F_1$ (590 nm) provides information about the site symmetry around Eu^{3+} ions. It turned out that the *R* value for Eu^{3+} at the surface site was smaller than that in the

interior region of TiO_2 [166]. Consequently, the decrease of *R* value together with the overall augment of PL emission intensity suggested that the emission of Eu^{3+} at the surface site of TiO_2 NCs was greatly improved with the increase of light induced surface defects, which undoubtedly indicated that the surface defect participated in and promoted the energy transfer process from TiO_2 host to Eu^{3+} ions.

In addition to acting as intermediate states to enhance the host-to-Ln^{3+} energy transfer, the defect may also play the role of the exciton traps in case of deep defects. The trapped excitons should be thermally released from the defect state prior to the energy transfer from the host to Ln^{3+} ions. When this defect trap of excitons becomes prominent, the de-trapping process will determine the de-excitation process of excitons, i.e., the PL lifetime of Ln^{3+} emitters will be significantly lengthened. In our recent work, host sensitized afterglow luminescence of Eu^{3+} in SnO_2 NCs was observed at the temperature below 250 K due to the capture of excitons in the deep defects during the energy transfer process [211]. Fig. 19a shows room-temperature PL excitation and emission spectra of Eu^{3+} in SnO_2 NCs. The bandgap absorption of SnO_2 NCs at 300 nm was found to dominate the excitation spectrum when monitoring the Eu^{3+} emission at 588 nm (Fig. 19a, left), indicating an efficient energy transfer process from host to Eu^{3+}. Sharp and well resolved emission lines of Eu^{3+} with the dominant $^5D_0 \rightarrow {}^7F_1$ transition lines at 588.0, 592.8 and 599.0 nm were observed in the emission spectrum, which obeyed the selection rule for the 4f-4f transitions of Eu^{3+} in centrosymmetric site (most likely to replace Sn^{4+} at D_{2h}), thereby confirming the incorporation of Eu^{3+} into the SnO_2 lattice sites. Fig. 19b illustrates the PL decays by monitoring the $^5D_0 \rightarrow {}^7F_1$ transition at 588 nm of Eu^{3+} in SnO_2:Eu^{3+} NCs at 100–300 K upon excitation above the bandgap energy at 300 nm. The PL decay at 300 K exhibited single exponential nature and PL lifetime of $^5D_0$ was fitted to be 15.9 ms. With the decrease of experimental temperature, the decay curves of Eu^{3+} were found to deviate from the single exponential, regardless of the low doping concentration (0.01 at.%). Moreover, an unusually long decay of Eu^{3+} even up to several tens of seconds was observed in the tail at temperature below 250 K, indicating the occurrence of long afterglow luminescence from the sample. The origin of long afterglow luminescence was verified from Eu^{3+} ions by the persistent emission spectra

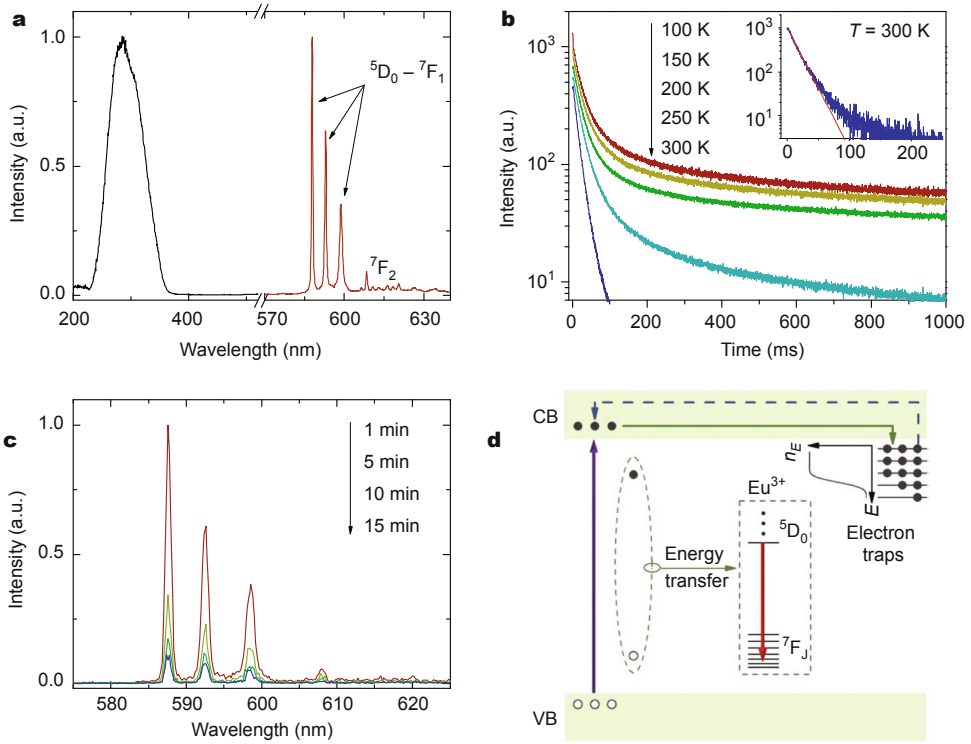

Figure 19 (a) Normalized PL excitation (λ_{em} = 588 nm) and emission (λ_{ex} = 300 nm) spectra of the SnO_2:Eu^{3+} NCs at 300 K. (b) Temperature-dependent PL decays of Eu^{3+} in the temperature range of 100–300 K. The inset shows the decay at 300 K and the fitting curve using single-exponential function (red line). (c) Persistent emission spectra of SnO_2:Eu^{3+} NPs acquired at 200 K and at different time intervals after the stoppage of excitation. (d) A schematic illustrtion of the persistent luminescence mechanism in SnO_2:Eu^{3+} NCs. Adapted with permission from Ref. [211]. Copyright 2015, the Royal Society of Chemistry.

in Fig. 19c, which exhibited essentially the same profile as that of the steady-state emission spectrum at different time intervals after the stoppage of excitation. The persistent luminescence of Eu^{3+} was further revealed to arise from the trap of electron in the CB by the deep defects below the CB prior to nonradiative transferring its energy to Eu^{3+} ions (Fig. 19d).

To overcome the concern of low solubility of Ln^{3+} in SNCs, more efforts have recently been devoted to designing new heterostructures such as isolator/semiconductor core-shell structure to spatially isolate the activators (Ln^{3+}) and sensitizers (SNCs) and thus to enhance the dopant concentration in the materials [212–214]. Generally, the Ln^{3+} ions are doped into the isolator layer in which the Ln^{3+} ions have high solubility due to the similar ionic radius and the same charge between dopants and host cations, and the semiconductor layer acts as sensitizers. For example, in Y_2O_3:Tb^{3+}, Yb^{3+}, Li^+/CdZnS core-shell heterostructures, the energy absorbed by CdZnS bandgap can be nonradiatively transferred to Tb^{3+} excited states in Y_2O_3 core, and the subsequent quantum cutting downconversion between Tb^{3+}-Yb^{3+} couples resulted in NIR emission of Yb^{3+}. Herein, Tb^{3+} acted as an energy bridge to mediate the energy transfer from CdZnS to Yb^{3+} ions (Fig. 20a). To verify this energy transfer, PL excitation, emission and excited state dynamics were investigated in detail (Figs 20b–e). Fig. 20b shows the NIR emission spectra under the excitation directly from the 4f-5d transition at 300 nm of Tb^{3+} or from band edge absorption at 472 nm of CdZnS. The PL intensity upon excitation above CdZnS bandgap was observed to be much stronger than that upon direct excitation, indicative of a more efficient excitation via host sensitization than via direct excitation. The energy transfer between the core and the shell was further confirmed by the excitation spectra in Fig. 20c. For core-only phosphors, a broad band at around 300 nm ascribed to the 4f-5d absorption of Tb^{3+} dominated the excitation spectrum by monitoring the 977 nm emission of Yb^{3+}. By contrast, after the growth of CdZnS shell, an intense excitation peak at 472 nm appeared in addition to the 300-nm excitation band (Fig. 20c). The main excitation peak at 472 nm proved to originate from the CdZnS bandgap absorption, suggesting that efficient energy transfer from CdZnS to Yb^{3+} ions occurred. In this case, Tb^{3+} ions were found to play the key role for the sensitized emission of Yb^{3+}, based on the fact that the Yb^{3+} emission decreased dramatically in the absence of Tb^{3+} (Fig. 20d). The energy transfer efficiency of $Tb^{3+}\rightarrow Yb^{3+}$ was determined by means of the excitation dynamic experiments, which was found to increase with the increasing concentration of Yb^{3+} and was estimated to be 56.4% when the Yb^{3+} concentration reached 10 mol.%. It should be noted that, in such core-shell heterostructures, only small part of activators located at the interface and adjacent to the energy donors participated in the light emission, which may greatly reduce the overall luminescent efficiency of materials.

CONCLUSIONS AND PERSPECTIVES

Ln^{3+} ions doped SNCs have been regarded as promising new-generation luminescent materials in view of the potential efficient energy transfer from SNCs host to Ln^{3+} ions. For the past decades, many efforts have been devoted to the material synthesis and optical property tuning of this kind of materials. It was found that by carefully controlling the synthesis strategies, Ln^{3+} can be effectively incorporated into the SNC host lattice via some wet chemical methods, e.g., sol-gel or hydro- (solvo-) thermal routes. Because of the large mismatch in ionic radius and charge imbalance between Ln^{3+} and the host cations, multiple sites possessing various CF surroundings were usually formed after the introduction of Ln^{3+} ions into the lattices of SNCs. These different luminescence centers of Ln^{3+} ions can be well identified with the aid of site-selective and time-resolved optical spectroscopy. The host-to-Ln^{3+} energy transfer could be readily achieved in the case that the energy levels of Ln^{3+} excited states match well with the bandgap energy of SNCs. The defect states or the co-doped guest ions were found to be effective in bridging the energy gap between the CB of SNCs and the excited states of Ln^{3+} ions, which might eventually enhance the host-to-Ln^{3+} energy transfer efficiency.

Although these findings are encouraging, some key challenges are still needed to be resolved for SNCs:Ln^{3+} in order to advance their potential applications in lighting, displays and biomedical fields. First, the luminescent efficiency or absolute quantum yield of SNCs:Ln^{3+} is still low, not ideal for practical applications. The improvement of the material crystallization and the introduction of proper charge compensators to reduce the defects in the SNCs system might be two effective strategies to improve the optical performance of SNCs:Ln^{3+}. Second, although a variety of approaches or techniques have been proposed to prepare Ln^{3+} ions doped SNCs, synthesizing monodisperse and size-controllable SNCs remains a challenge so far. More efforts are required to develop simple but feasible synthetic protocols for fabricating monodisperse Ln^{3+} ions doped SNCs with desired physicochemical properties, which is currently of particular interest for their further technological applications as versatile nano-bioprobes. Last but not the least, an important and unique merit of SNCs:Ln^{3+}, different from the other luminescent materials, is their potential ability to tune the optical properties of Ln^{3+} via

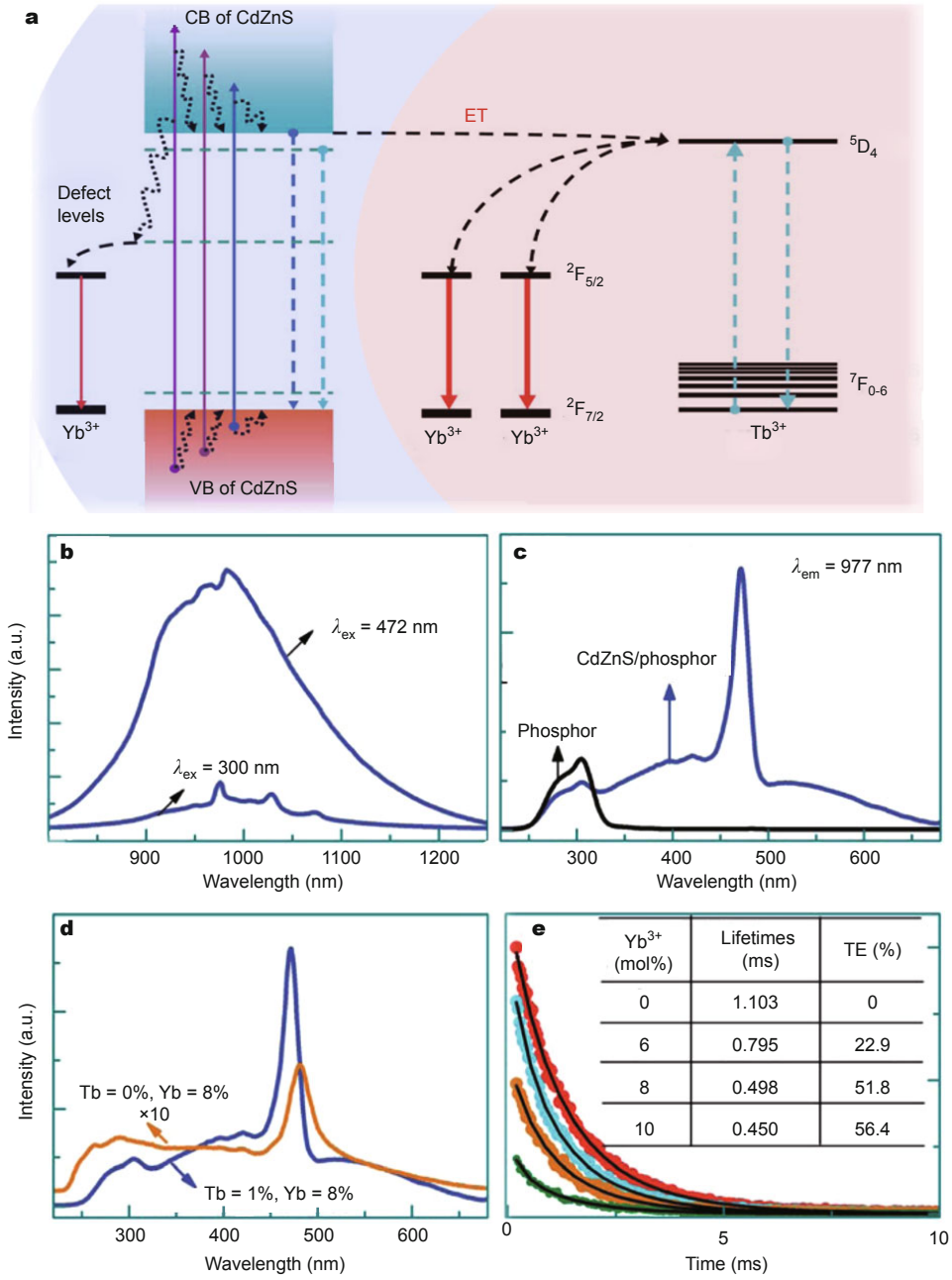

Yb^{3+} (mol%)	Lifetimes (ms)	TE (%)
0	1.103	0
6	0.795	22.9
8	0.498	51.8
10	0.450	56.4

Figure 20 (a) A schematic illustration of energy transfer process from the CdZnS shell to Y_2O_3:Tb^{3+}, Yb^{3+} core particles; (b) emission spectra of Y_2O_3:Tb^{3+}, Yb^{3+}/CdZnS under the excitation at 300 and 472 nm, respectively; (c) excitation spectra of the core-shell heterostructures and the core-only phosphor; (d) comparison of excitation spectra between the samples with and without Tb doping; (e) PL decays of Tb^{3+} by monitoring the 544-nm emission in the core-shell sample with variousYb^{3+} contents. Adapted with permission from Ref. [213]. Copyright 2015, the Royal Society of Chemistry.

the bandgap engineering of SNCs, which is a facile and effective approach to further optimizing the optical performance of the materials. Nevertheless, such kind of work remains nearly untouched hitherto.

Received 6 September, 2015; accepted 21 September, 2015; published online 23 October 2015

1 Deng ML, Wang LY. Unexpected luminescence enhancement of upconverting nanocrystals by cation exchange with well retained small particle size. Nano Res, 2014, 7: 782–793
2 Deng ML, Ma YX, Huang S, Hu GF, Wang LY. Monodisperse upconversion $NaYF_4$ nanocrystals: syntheses and bioapplications. Nano Res, 2011, 4: 685–694
3 Dong H, Sun LD, Yan CH. Energy transfer in lanthanide upconver-

sion studies for extended optical applications. Chem Soc Rev, 2015, 44: 1608–1634
4 Dong H, Du SR, Zheng XY, *et al*. Lanthanide nanoparticles: from design toward bioimaging and therapy. Chem Rev, 2015, 115: 10725–10815
5 Shang MM, Li CX, Lin J. How to produce white light in a single-phase host? Chem Soc Rev, 2014, 43: 1372–1386
6 Hou ZY, Zhang YX, Deng KR, *et al*. UV-emitting upconversion-based TiO_2 photosensitizing nanoplatform: near-infrared light mediated *in vivo* photodynamic therapy via mitochondria-involved apoptosis pathway. ACS nano, 2015, 9: 2584–2599
7 Deng RR, Qin F, Chen RF, *et al*. Temporal full-colour tuning through non-steady-state upconversion. Nat Nanotechnol, 2015, 10: 237–242
8 Liu XG, Yan CH, Capobianco JA. Photon upconversion nanomaterials. Chem Soc Rev, 2015, 44: 1299–1301
9 Huang P, Tu DT, Zheng W, *et al*. Inorganic lanthanide nanoprobes for background-free luminescent bioassays. Sci China Mater, 2015, 58: 156–177
10 Yu XF, Li M, Xie MY, *et al*. Dopant-controlled synthesis of water-soluble hexagonal $NaYF_4$ nanorods with efficient upconversion fluorescence for multicolor bioimaging. Nano Res, 2010, 3: 51–60
11 Wang L, Zhang Y, Zhu Y. One-pot synthesis and strong near-infrared upconversion luminescence of poly(acrylic acid)-functionalized YF^3:Yb^{3+}/Er^{3+} nanocrystals. Nano Res, 2010, 3: 317–325
12 Cheng L, Yang K, Zhang S, *et al*. Highly-sensitive multiplexed *in vivo* imaging using PEGylated upconversion nanoparticles. Nano Res, 2010, 3: 722–732
13 Prasad PN. Nanophotonics. New York: John Wiley & Sons, 2004
14 Bol AA, van Beek R, Meijerink A. On the incorporation of trivalent rare earth ions in II–VI semiconductor nanocrystals. Chem Mater, 2002, 14: 1121–1126
15 Pandey P, Kurchania R, Haque FZ. Optical studies of europium-doped ZnO nanoparticles prepared by sol-gel technique. J Adv Phys, 2014, 3: 104–110
16 Tanner PA, Yu LX. Photoluminescence of ZnO:Eu^{3+} nanoflowers. J Nanosci Nanotechnol, 2008, 8: 1307–1311
17 Armelao L, Bottaro G, Pascolini M, *et al*. Structure-luminescence correlations in europium-doped sol-gel ZnO nanopowders. J Phys Chem C, 2008, 112: 4049–4054
18 Wang N, Lin H, Li JB, Yang XZ, Zhang LZ. Photoluminescence of TiO_2:Eu nanotubes prepared by a two-step approach. J Lumin, 2007, 122: 889–891
19 Wang J, Zhou MJ, Hark SK, *et al*. Local electronic structure and luminescence properties of Er doped ZnO nanowires. Appl Phys Lett, 2006, 89: 221917
20 Liu YS, Li RF, Luo WQ, Zhu HM, Chen XY. Optical spectroscopy of Sm^{3+} and Dy^{3+} doped ZnO nanocrystals. Spectrosc Lett, 2010, 43: 343–349
21 Kar A, Patra A. Optical and electrical properties of Eu^{3+}-doped SnO_2 nanocrystals. J Phys Chem C, 2009, 113: 4375–4380
22 Sun YJ, Chen Y, Tian LJ, *et al*. Morphology-dependent upconversion luminescence of ZnO:Er^{3+} nanocrystals. J Lumin, 2008, 128: 15–21
23 Li JG, Wang XH, Watanabe K, Ishigaki T. Phase structure and luminescence properties of Eu^{3+}-doped TiO_2 nanocrystals synthesized by Ar/O_2 radio frequency thermal plasma oxidation of liquid precursor mists. J Phys Chem B, 2006, 110: 1121–1127
24 Liu YS, Luo WQ, Li RF, Chen XY. Optical properties of Nd^{3+} ion-doped ZnO nanocrystals. J Nanosci Nanotechnol, 2010, 10: 1871–1876
25 Mukherjee P, Shade CM, Yingling AM, *et al*. Lanthanide sensitization in II-VI semiconductor materials: a case study with terbium(III) and europium(III) in zinc sulfide nanoparticles. J Phys Chem A, 2011, 115: 4031–4041
26 Liang ZG, Mu J, Han L, Yu HQ. Microbe-assisted synthesis and luminescence properties of monodispersed Tb^{3+}-doped ZnS nanocrystals. J Nanomater, 2015, 2015: 519303
27 Mukherjee P, Sloan RF, Shade CM, Waldeck DH, Petoud S. A postsynthetic modification of II–VI semiconductor nanoparticles to create Tb^{3+} and Eu^{3+} luminophores. J Phys Chem C, 2013, 117: 14451–14460
28 Liu YS, Zhou SY, Tu DT, *et al*. Amine-functionalized lanthanide-doped zirconia nanoparticles: optical spectroscopy, time-resolved fluorescence resonance energy transfer biodetection, and targeted imaging. J Am Chem Soc, 2012, 134: 15083–15090
29 Vela J, Prall BS, Rastogi P, *et al*. Sensitization and protection of lanthanide ion emission in In_2O_3:Eu nanocrystal quantum dots. J Phys Chem C, 2008, 112: 20246–20250
30 Ghatak A, Debnath GH, Mandal M, Mukherjee P. Lanthanide cation-induced tuning of surface capping properties in zinc sulfide nanoparticles: an infrared absorption study. RSC Adv, 2015, 5: 32920–32932
31 Bishnoi S, Das R, Chawla S. Gold nanosphere enhanced green and red fluorescence in ZnO:Al, Eu^{3+}. Appl Phys Lett, 2014, 105: 233108
32 Geburt S, Lorke M, da Rosa AL, *et al*. Intense intrashell luminescence of Eu-doped single ZnO nanowires at room temperature by implantation created Eu–Oi complexes. Nano Lett, 2014, 14: 4523–4528
33 Yang S, Han DL, Gao M, Yang JH, Bayanheshig. Controllable morphology and tunable colors of Mg and Eu ion co-doped ZnO by thermal annealing. CrystEngComm, 2014, 16: 6896–6900
34 Schäfer H, Hess C, Tobergte H, *et al*. Ultrafine sanding paper: a simple tool for creating small particles. Small, 2015, 11: 931–935
35 Yin JB, Xiang LQ, Zhao XP. Monodisperse spherical mesoporous Eu-doped TiO_2 phosphor particles and the luminescence properties. Appl Phys Lett, 2007, 90: 113112
36 Pereira AS, Peres M, Soares MJ, *et al*. Synthesis, surface modification and optical properties of Tb^{3+}-doped ZnO nanocrystals. Nanotechnology, 2006, 17: 834–839
37 Li L, Tsung CK, Yang Z, *et al*. Rare-earth-doped nanocrystalline titania microspheres emitting luminescence via energy transfer. Adv Mater, 2008, 20: 903–908
38 Du YP, Zhang YW, Sun LD, Yan CH. Efficient energy transfer in monodisperse Eu-doped ZnO nanocrystals synthesized from metal acetylacetonates in high-boiling solvents. J Phys Chem C, 2008, 112: 12234–12241
39 Das S, Mandal KC. Optical down-conversion in doped ZnSe:Tb^{3+} nanocrystals. Nanoscale, 2013, 5: 913–915
40 Chen W, Zhang JZ, Joly AG. Optical properties and potential applications of doped semiconductor nanoparticles. J Nanosci Nanotechnol, 2004, 4: 919–947
41 Liu YS, Luo WQ, Zhu HM, Chen XY. Optical spectroscopy of lanthanides doped in wide band-gap semiconductor nanocrystals. J Lumin, 2011, 131: 415–422
42 Chen XY, Luo WQ, Liu YS, Liu GK. Recent progress on spectroscopy of santhanide ions incorporated in semiconductor nanocrystals. J Rare Earths, 2007, 25: 515–525
43 O'Donnell KP. The temperature dependence of the luminescence of rare-earth-doped semiconductors: 25 years after Favennec. Phys Status Solidi C, 2015, 12: 466–468
44 Xiao QB, Zhu HM, Tu DT, Ma E, Chen XY. Near-infrared-to-near-infrared downshifting and near-infrared-to-visible upconverting luminescence of Er^{3+}-doped In_2O_3 nanocrystals. J Phys Chem C, 2013, 117: 10834–10841
45 Lide DR. CRC Handbook of Chemistry and Physics (74th eds.).

Boca Raton: CRC, 1993–1994
46 Yang L, Dong JZ, She YJ, *et al*. Self-purification construction of interstitial O in the neighbor of Eu^{3+} ions to act as energy transfer bridge. Appl Phys Lett, 2014, 104: 033109
47 Chen GY, Zhang YG, Somesfalean G, *et al*. Two-color upconversion in rare-earth-ion-doped ZrO_2 nanocrystals. Appl Phys Lett, 2006, 89: 163105
48 Aneesh PM, Jayaraj MK. Red luminescence from hydrothermally synthesized Eu-doped ZnO nanoparticles under visible excitation. Bull Mater Sci, 2010, 33: 227–231
49 Zeng XY, Yuan JL, Wang ZY, Zhang L. Nanosheet-based microspheres of Eu^{3+}-doped ZnO with efficient energy transfer from ZnO to Eu^{3+} at room temperature. Adv Mater, 2007, 19: 4510–4514
50 Tamm A, Kemell M, Kozlova J, *et al*. Atomic layer deposition and characterization of erbium oxide-doped zirconium oxide thin films. J Electrochem Soc, 2010, 157: G193–G201
51 Ji SL, Yin LL, Liu GD, Zhang LD, Ye CH. Synthesis of rare earth ions-doped ZnO nanostructures with efficient host-guest energy transfer. J Phys Chem C, 2009, 113: 16439–16444
52 Chen XB, Li LP, Su YG, Li GS. Phase evolution and photoluminescence of Eu^{3+}-doped ZrO_2. J Nanosci Nanotechnol, 2010, 10: 1800–1807
53 Fidelus JD, Yatsunenko S, Godlewski M, *et al*. Relation between structural properties of Pr^{3+}-doped yttria-stabilized zirconia nanopowders and their luminescence efficiency. Scripta Mater, 2009, 61: 415–418
54 Chen LM, Liu YN, Li YD. Preparation and characterization of ZrO_2:Eu^{3+} phosphors. J Alloy Compd, 2004, 381: 266–271
55 Li GR, Dawa CR, Lu XH, Yu XL, Tong YX. Use of additives in the electrodeposition of nanostructured Eu^{3+}/ZnO films for photoluminescent devices. Langmuir, 2009, 25: 2378–2384
56 Lue Q, Guo FY, Sun L, Li AH, Zhao LC. Surface modification of ZrO_2:Er^{3+} nanoparticles to attenuate aggregation and enhance upconversion fluorescence. J Phys Chem C, 2008, 112: 2836–2844
57 Zeng XY, Yuan JL, Zhang L. Synthesis and photoluminescent properties of rare earth doped ZnO hierarchical microspheres. J Phys Chem C, 2008, 112: 3503–3508
58 Xue DQ, Zhang JY, Yang C, Wang TM. PL and EL characterizations of ZnO:Eu^{3+} Li^+ films derived by sol-gel process. J Lumin, 2008, 128: 685–689
59 Liu YS, Luo WQ, Li RF, *et al*. Optical spectroscopy of Eu^{3+} doped ZnO nanocrystals. J Phys Chem C, 2008, 112: 686–694
60 Liu L, Wang YX, Bai YF, *et al*. Single band upconversion mechanisms of Er^{3+}/Yb^{3+}:ZrO_2 nanocrystals. Opt Commun, 2012, 285: 1528–1532
61 Gomez LA, Menezes LD, de Araujo CB, *et al*. Upconversion luminescence in Er^{3+} doped and Er^{3+}/Yb^{3+} codoped zirconia and hafnia nanocrystals excited at 980 nm. J Appl Phys, 2010, 107: 113508
62 Diaz-Torres LA, De la Rosa E, Salas P, Romero VH, Angeles-Chavez C. Efficient photo luminescence of Dy^{3+} at low concentrations in nanocrystalline ZrO_2. J Solid State Chem, 2008, 181: 75–80
63 De la Rosa E, Diaz-Torres LA, Salas P, Rodriguez RA. Visible light emission under UV and IR excitation of rare earth doped ZrO_2 nanophosphor. Opt Mater, 2005, 27: 1320–1325
64 Han HL, Yang LW, Liu YX, Zhang YY, Yang QB. Up-conversion luminescence switching in Er^{3+}-containing ZnO nanoparticles through Li^+ co-doping. Opt Mater, 2008, 31: 338–341
65 Cheng BM, Yu LX, Duan CK, Wang HS, Tanner PA. Vacuum ultraviolet and visible spectra of ZnO:Eu^{3+} prepared by combustion synthesis. J Phys-Condens Mat, 2008, 20: 345231–345234
66 Rinnert H, Miska P, Vergnat M, *et al*. Photoluminescence of Nd-doped SnO_2 thin films. Appl Phys Lett, 2012, 100: 101908
67 Strauss M, Destefani TA, Sigoli FA, Mazali IO. Crystalline SnO_2 nanoparticles size probed by Eu^{3+} luminescence. Cryst Growth Des, 2011, 11: 4511–4516
68 Armelao L, Heigl F, Jurgensen A, *et al*. X-ray excited optical luminescence studies of ZnO and Eu-doped ZnO nanostructures. J Phys Chem C, 2007, 111: 10194–10200
69 Kong JT, Zhu HM, Li RF, Luo WQ, Chen XY. Carrier-mediated 1.55 μm photoluminescence from single Er^{3+} center in SnO_2 nanocrystals. Opt Lett, 2009, 34: 1873–1875
70 Moon T, Hwang ST, Jung DR, *et al*. Hydroxyl-quenching effects on the photoluminescence properties of SnO_2:Eu^{3+} nanoparticles. J Phys Chem C, 2007, 111: 4164–4167
71 Wang H, Wang Y, Kershaw SV, *et al*. Fluorinated Eu-doped SnO_2 nanostructures with simultaneous phase and shape control and improved photoluminescence. Part Part Syst Char, 2013, 30: 332–337
72 Monteiro T, Neves AJ, Soares MJ, *et al*. Up conversion from visible to ultraviolet in bulk ZnO implanted with Tm ions. Appl Phys Lett, 2005, 87: 192108
73 Jia WY, Monge K, Fernandez F. Energy transfer from the host to Eu^{3+} in ZnO. Opt Mater, 2003, 23: 27–32
74 Brovelli S, Chiodini A, Lauria A, Meinardi F, Paleari A. Energy transfer to erbium ions from wide-band-gap SnO_2 nanocrystals in silica. Phys Rev B, 2006, 73: 073406
75 Del Castillo J, Rodriguez VD, Yanes AC, Mendez-Ramos J, Torres ME. Luminescent properties of transparent nanostructured Eu^{3+} doped SnO_2-SiO_2 glass-ceramics prepared by the sol-gel method. Nanotechnology, 2005, 16: S300–S303
76 Nogami M, Ohno A, You HP. Laser-induced SnO_2 crystallization and fluorescence properties in Eu^{3+}-doped SnO_2-SiO_2 glasses. Phys Rev B, 2003, 68: 104204
77 Kiisk V, Kangur T, Paalo M, *et al*. Structural and luminescence characteristics of SnO_2:Eu and SnO_2:Eu,Sb nanophosphors upon annealing at high temperatures. Mater Chem Phys, 2011, 130: 293–298
78 Sambasivam S, Kim SB, Jeong JH, *et al*. Effect of Er^{3+} doping in SnO_2 semiconductor nanoparticles synthesized by sol-gel technique. Curr Appl Phys, 2010, 10: 1383–1386
79 Bouzidi C, Elhouichet H, Moadhen A. Yb^{3+} effect on the spectroscopic properties of Er-Yb codoped SnO_2 thin films. J Lumin, 2011, 131: 2630–2635
80 Ishizumi A, Kanemitsu Y. Structural and luminescence properties of Eu-doped ZnO nanorods fabricated by a microemulsion method. Appl Phys Lett, 2005, 86: 253106
81 Wei XJ, Wang W, Chen KZ. ZnO:Er,Yb,Gd particles designed for magnetic-fluorescent imaging and near-infrared light triggered photodynamic therapy. J Phys Chem C, 2013, 117: 23716–23729
82 Pal P, Manam J. Color tunable ZnO nanorods by Eu^{3+} and Tb^{3+} co-doping for optoelectronic applications. Appl Phys A, 2014, 116: 213–223
83 Zhu HM, Li RF, Luo WQ, Chen XY. Eu^{3+}-doped beta-Ga_2O_3 nanophosphors: annealing effect, electronic structure and optical spectroscopy. Phys Chem Chem Phys, 2011, 13: 4411–4419
84 Biljan T, Gajovic A, Meic Z. Visible and NIR luminescence of nanocrystalline beta-Ga_2O_3:Er^{3+} prepared by solution combustion synthesis. J Lumin, 2008, 128: 377–382
85 Hirata GA, Ramos F, Garcia R, *et al*. A new combustion synthesis method for GaN:Eu^{3+} and Ga_2O_3:Eu^{3+} luminescent powders. Phys Status Solidi A, 2001, 188: 179–182
86 Yue D, Lu W, Jin L, *et al*. Controlled synthesis, asymmetrical transport behavior and luminescence properties of lanthanide doped ZnO mushroom-like 3D hierarchical structures. Nanoscale, 2014, 6: 13795–13802
87 Zhao JG, Zhang WY, Xie EQ, *et al*. Structure and photoluminescence of beta-Ga_2O_3:Eu^{3+} nanofibers prepared by electrospinning. Appl Surf Sci, 2011, 257: 4968–4972

88 Kumar V, Kumar V, Som S, *et al*. Effect of Eu doping on the photoluminescence properties of ZnO nanophosphors for red emission applications. Appl Surf Sci, 2014, 308: 419–430
89 Gu F, Wang SF, Lu MK, *et al*. Structure evaluation and highly enhanced luminescence of Dy^{3+}-doped ZnO nanocrystals by Li^{+} doping via combustion method. Langmuir, 2004, 20: 3528–3531
90 Li GG, Peng C, Li CX, *et al*. Shape-controllable synthesis and morphology-dependent luminescence properties of GaOOH:Dy^{3+} and beta-Ga_2O_3:Dy^{3+}. Inorg Chem, 2010, 49: 1449–1457
91 Niu JH, Hua RN, Li WL, Li MT, Yu TZ. Electroluminescent properties of a device based on terbium-doped ZnS nanocrystals. J Phys D Appl Phys, 2006, 39: 2357–2360
92 Chen W, Joly AG, Malm JO, Bovin JO. Upconversion luminescence of Eu^{3+} and Mn^{2+} in ZnS:Mn^{2+}, Eu^{3+} codoped nanoparticles. J Appl Phys, 2004, 95: 667–672
93 Ahemen I, Amah A, AttahDaniel B, Fasasi A. Spherical nanoparticles of Eu $^{3+}$-doped ZnS semiconductor synthesized from ZnO nanorods precursor. Nanosci Nanotechno, 2014, 4: 7–15
94 Wei XJ, Wang W, Chen KZ. Preparation and characterization of ZnS:Tb,Gd and ZnS:Er,Yb,Gd nanoparticles for bimodal magnetic-fluorescent imaging. Dalton T, 2013, 42: 1752–1759
95 Sinha G, Patra A. Generation of green, red and white light from rare-earth doped Ga_2O_3 nanoparticles. Chem Phys Lett, 2009, 473: 151–154
96 Liu GC, Duan XC, Li HB, Liang D. Preparation and photoluminescence properties of Eu-doped Ga_2O_3 nanorods. Mater Chem Phys, 2008, 110: 206–211
97 Hou SL, Yuen YY, Mao HB, Wang JQ, Zhu ZQ. Photoluminescence properties of the Eu^{3+}-doped ZnS nanocrystals and the crystal-field analysis. J Phys D-Appl Phys, 2009, 42: 215105
98 Nogales E, Mendez B, Piqueras J, Garcia JA. Europium doped gallium oxide nanostructures for room temperature luminescent photonic devices. Nanotechnology, 2009, 20: 115201
99 Nogales E, Garcia JA, Mendez B, Piqueras J. Doped gallium oxide nanowires with waveguiding behavior. Appl Phys Lett, 2007, 91: 133108
100 Liu XM, Yu CC, Li CX, Lin J. Comparative study of Ga_2O_3:Dy^{3+} phosphors prepared by three methods. J Electrochem Soc, 2007, 154: P86–P91
101 Wang YJ, Wu CX, Chen MZ, Huang MC. Dynamical analysis of relaxation luminescence in ZnS:Er^{3+} thin film devices. J Appl Phys, 2003, 93: 9625–9629
102 Kim JS, Kim HE, Kwon AK, Park HL, Kim GC. Effect of initial pH on nanophosphor β-Ga_2O_3:Eu^{3+} prepared through sol-gel process. J Lumin, 2007, 122: 710–713
103 Shen WY, Pang ML, Lin J, Fang J. Host-sensitized luminescence of Dy^{3+} in nanocrystalline β-Ga_2O_3 prepared by a Pechini-type sol-gel process. J Electrochem Soc, 2005, 152: H25–H28
104 Pang ML, Shen WY, Lin J. Enhanced photoluminescence of Ga_2O_3:Dy^{3+} phosphor films by Li^{+} doping. J Appl Phys, 2005, 97: 033511
105 Kim JS, Kim HE, Park HL, Kim GC. Luminescence intensity and color purity enhancement in nanostructured β-Ga_2O_3:Eu^{3+} phosphors. Solid State Commun, 2004, 132: 459–463
106 Georgobiani AN, Kotljarevsky MB, Kidalov VV, Rogozin IV, Aminov UA. p-type II-VI compounds doped by rare-earth elements. J Cryst Growth, 2000, 214: 516–519
107 Hao JH, Lou ZD, Renaud I, Cocivera M. Electroluminescence of europium-doped gallium oxide thin films. Thin Solid Films, 2004, 467: 182–185
108 Hao JH, Cocivera M. Optical and luminescent properties of undoped and rare-earth-doped Ga_2O_3 thin films deposited by spray pyrolysis. J Phys D-Appl Phys, 2002, 35: 433–438
109 Lin T, Ding XY, Xu J, *et al*. Influences of doping and annealing conditions on the photoluminescence from In_2O_3 nanocrystals and Eu^{3+} ions co-doped sol-gel SiO_2 films. J Appl Phys, 2011, 109: 083512
110 Jin BK, Kim JK, Yu SM, Choi YG. Electrical and optical properties of Er^{3+}-doped indium tin oxide thin films fabricated via a sol-gel technique. J Ceram Process Res, 2009, 10: S26–S31
111 Podhorodecki A, Kudrawiec R, Misiewicz J, Gaponenko NV, Tsyrkunov DA. 1.54 μm photoluminescence from Er-doped sol-gel derived In_2O_3 films embedded in porous anodic alumina. Opt Mater, 2006, 28: 685–687
112 Deng L, Shan Y, Xu JJ, Chen HY. Electrochemiluminescence behaviors of Eu^{3+}-doped CdS nanocrystals film in aqueous solution. Nanoscale, 2012, 4: 831–836
113 Planelles-Arago J, Cordoncillo E, Ferreira RAS, Carlos LD, Escribano P. Synthesis, characterization and optical studies on lanthanide-doped CdS quantum dots: new insights on CdS→lanthanide energy transfer mechanisms. J Mater Chem, 2011, 21: 1162–1170
114 Chowdhury PS, Patra A. Role of dopant concentration and surface coating on photophysical properties of CdS:Eu^{3+} nanocrystals. Phys Chem Chem Phys, 2006, 8: 1329–1334
115 Xiao QB, Liu YS, Liu LQ, *et al*. Eu^{3+}-doped In_2O_3 nanophosphors: electronic structure and optical characterization. J Phys Chem C, 2010, 114: 9314–9321
116 Zou SY, Meng JX. Synthesis and upconversion luminescence of Er^{3+}/Yb^{3+} co-doped In_2O_3 nanocrystals. Chinese J Inorg Chem, 2011, 27: 1138–1142
117 Zhang KX, Yu YX, Sun SQ. Influence of Eu doping on the microstructure and photoluminescence of CdS nanocrystals. Appl Surf Sci, 2012, 258: 7658–7663
118 Yu YL, Chen DQ, Wang YS, *et al*. Enhanced photoluminescence of Eu^{3+} induced by energy transfer from In_2O_3 nano-crystals embedded in glassy matrix. Phys Chem Chem Phys, 2009, 11: 8774–8778
119 Rai S, Bokatial L, Dihingia PJ. Effect of CdS nanoparticles on fluorescence from Sm^{3+} doped SiO_2 glass. J Lumin, 2011, 131: 978–983
120 Bokatial L, Rai S. Optical properties and up-conversion of Pr^{3+} doped CdS nanoparticles in sol-gel glasses. J Lumin, 2010, 130: 1857–1862
121 Planelles-Arago J, Julian-Lopez B, Cordoncillo E, *et al*. Lanthanide doped ZnS quantum dots dispersed in silica glasses: an easy one pot sol-gel synthesis for obtaining novel photonic materials. J Mater Chem, 2008, 18: 5193–5199
122 Julian B, Planelles J, Cordoncillo E, *et al*. Eu^{3+}-doped CdS nanocrystals in SiO_2 matrices: one-pot sol-gel synthesis and optical characterization. J Mater Chem, 2006, 16: 4612–4618
123 Lee DG, Nishikawa A, Terai Y, Fujiwara Y. Eu luminescence center created by Mg codoping in Eu-doped GaN. Appl Phys Lett, 2012, 100: 171904
124 Jia CW, Xie EQ, Zhao JG, Sun ZW, Peng AH. Visible and near-infrared photoluminescences of europium-doped titania film. J Appl Phys, 2006, 100: 023529
125 Bahtat A, Bouazaoui M, Bahtat M, *et al*. Up-conversion fluorescence spectroscopy in Er^{3+}:TiO_2 planar waveguides prepared by a sol-gel process. J Non-Cryst Solids, 1996, 202: 16–22
126 Setiawati E, Kawano K. Stabilization of anatase phase in the rare earth; Eu and Sm ion doped nanoparticle TiO_2. J Alloy Compd, 2008, 451: 293–296
127 Frindell KL, Bartl MH, Popitsch A, Stucky GD. Sensitized luminescence of trivalent europium by three-dimensionally arranged anatase nanocrystals in mesostructured titania thin films. Angew Chem Int Edit, 2002, 41: 959–962
128 Zhao XP, Yin JB. Preparation and electrorheological characteristics of rare-earth-doped TiO_2 suspensions. Chem Mater, 2002, 14: 2258–2263
129 Conde-Gallardo A, Garcia-Rocha M, Hernandez-Calderon I, Palo-

mino-Merino R. Photoluminescence properties of the Eu^{3+} activator ion in the TiO_2 host matrix. Appl Phys Lett, 2001, 78: 3436–3438
130 Conde-Gallardo A, Garcia-Rocha M, Palomino-Merino R, Velasquez-Quesada MP, Hernandez-Calderon I. Photoluminescence properties of Tb^{3+} and Eu^{3+} ions hosted in TiO_2 matrix. Appl Surf Sci, 2003, 212: 583–588
131 Palomino-Merino R, Conde-Gallardo A, Garcia-Rocha M, *et al*. Photoluminescence of TiO_2:Eu^{3+} thin films obtained by sol-gel on Si and Corning glass substrates. Thin Solid Films, 2001, 401: 118–123
132 Gao CM, Song HW, Hu LY, *et al*. Luminescence enhancement in bromine and samarium co-doped TiO_2 semiconductor nanocrystalline powders. J Lumin, 2008, 128: 559–564
133 Shang QK, Yu H, Kong XG, *et al*. Green and red up-conversion emissions of Er^{3+}-Yb^{3+} co-doped TiO_2 nanocrystals prepared by sol-gel method. J Lumin, 2008, 128: 1211–1216
134 Ting CC, Chen SY, Hsieh WF, Lee HY. Effects of yttrium codoping on photoluminescence of erbium-doped TiO_2 films. J Appl Phys, 2001, 90: 5564–5569
135 Ghosh P, Patra A. Influence of surface coating on physical properties of TiO_2/Eu^{3+} nanocrystals. J Phys Chem C, 2007, 111: 7004–7010
136 Fu CY, Liao JS, Luo WQ, Li RF, Chen XY. Emission of 1.53 μm originating from the lattice site of Er^{3+} ions incorporated in TiO_2 nanocrystals. Opt Lett, 2008, 33: 953–955
137 Takagi Y, Suwa T, Sekiguchi H, Okada H, Wakahara A. Effect of Mg codoping on Eu^{3+} luminescence in GaN grown by ammonia molecular beam epitaxy. Appl Phys Lett, 2011, 99: 171905
138 Wang R, Steckl AJ. Effect of growth conditions on Eu^{3+} luminescence in GaN. J Cryst Growth, 2010, 312: 680–684
139 Higuchi S, Ishizumi A, Sawahata J, Akimoto K, Kanemitsu Y. Luminescence and energy-transfer mechanisms in Eu^{3+}-doped GaN epitaxial films. Phys Rev B, 2010, 81: 035207
140 Wang R, Steckl AJ, Brown EE, Hommerich U, Zavada JM. Effect of Si codoping on Eu^{3+} luminescence in GaN. J Appl Phys, 2009, 105: 043107
141 Peng H, Lee CW, Everitt HO, *et al*. Spectroscopic and energy transfer studies of Eu^{3+} centers in GaN. J Appl Phys, 2007, 102: 073520
142 Sawahata J, Seo J, Chen SQ, *et al*. Photoluminescence spectra of Eu-doped GaN with various Eu concentrations. Appl Phys Lett, 2006, 89: 192104
143 Ishizumi A, Sawahata J, Akimoto K, Kanemitsu Y. Origin of efficient luminescence from GaN:Eu^{3+} epitaxial films revealed by microscopic photoluminescence imaging spectroscopy. Appl Phys Lett, 2006, 89: 191908
144 Andreev T, Liem NQ, Hori Y, *et al*. Optical transitions in Eu^{3+} ions in GaN:Eu grown by molecular beam epitaxy. Phys Rev B, 2006, 73: 195203
145 Peng HY, Lee CW, Everitt HO, *et al*. Effect of optical excitation energy on the red luminescence of Eu^{3+} in GaN. Appl Phys Lett, 2005, 86: 051110
146 Andreev T, Monroy E, Gayral B, *et al*. Eu locations in Eu-doped in GaN/GaN quantum dots. Appl Phys Lett, 2005, 87: 021906
147 Nyein EE, Hommerich U, Heikenfeld J, *et al*. Spectral and time-resolved photoluminescence studies of Eu-doped GaN. Appl Phys Lett, 2003, 82: 1655–1657
148 Heikenfeld J, Garter M, Lee DS, Birkhahn R, Steckl AJ. Red light emission by photoluminescence and electroluminescence from Eu-doped GaN. Appl Phys Lett, 1999, 75: 1189–1191
149 Gruber JB, Zandi B, Lozykowski HJ, Jadwisienczak WM. Spectroscopic properties of $Sm^{3+}(4f^5)$ in GaN. J Appl Phys, 2002, 91: 2929–2935
150 Park JH, Steckl AJ. Site specific Eu^{3+} stimulated emission in GaN host. Appl Phys Lett, 2006, 88: 011111
151 Yu HK, Yi GR, Kang JH, *et al*. Surfactant-assisted synthesis of uniform titania microspheres and their clusters. Chem Mater, 2008, 20: 2704–2710
152 Roqan IS, O'Donnell KP, Martin RW, *et al*. Identification of the prime optical center in GaN:Eu^{3+}. Phys Rev B, 2010, 81: 085209
153 Stouwdam JW, van Veggel FCJM. Sensitized emission in Ln^{3+}-doped TiO_2 semiconductor nanoparticles. Chem Phys Chem, 2004, 5: 743–746
154 Nyk M, Kudrawiec R, Strek W, Misiewicz J. Synthesis and optical properties of Eu^{3+} and Tb^{3+} doped GaN nanocrystallite powders. Opt Mater, 2006, 28: 767–770
155 Ji TH, Liu Y, Zhao H, *et al*. Preparation and up-conversion fluorescence of rare earth (Er^{3+} or Yb^{3+}/Er^{3+})-doped TiO_2 nanobelts. J Solid State Chem, 2010, 183: 584–589
156 Jeon S, Braun PV. Hydrothermal synthesis of Er-doped luminescent TiO_2 nanoparticles. Chem Mater, 2003, 15: 1256–1263
157 Qi XF, Song YH, Sheng Y, *et al*. Controllable synthesis and luminescence properties of TiO_2:Eu^{3+} nanorods, nanoparticles and submicrospheres by hydrothermal method. Opt Mater, 2014, 38: 193–197
158 Vranješ M, Kuljanin-Jakovljević J, Ahrenkiel S, *et al*. Sm^{3+} doped TiO_2 nanoparticles synthesized from nanotubular precursors-luminescent and structural properties. J Lumin, 2013, 143: 453–458
159 Kudrawiec R, Nyk M, Podhorodecki A, *et al*. Change in photoluminescence spectra of Eu-doped GaN powders due to the aggregation of nanosized grains into micrometer-sized conglomerations. Appl Phys Lett, 2006, 88: 061916
160 Park DJ, Sekino T, Tsukuda S, *et al*. Photoluminescence of samarium-doped TiO_2 nanotubes. J Solid State Chem, 2011, 184: 2695–2700
161 Liu FS, Liu QL, Liang JK, *et al*. Structure and visible photoluminescence of Sm^{3+}, Dy^{3+} and Tm^{3+} doped *c*-axis oriented AlN films. Chinese Phys, 2006, 15: 2445–2449
162 Zhao X, Ikegami K, Ishiwata S, *et al*. Photoluminescence and local structure analysis of Sm^{3+} ions in single phase TiO_2 thin films. AIP Conf Proc, 2011, 1399: 485–486
163 Vetter U, Gruber JB, Nijjar AS, *et al*. Crystal field analysis of Pm^{3+} ($4f^4$) and Sm^{3+} ($4f^5$) and lattice location studies of Nd-147 and Pm-147 in w-AlN. Phys Rev B, 2006, 74: 205201
164 Ikeda M, Li JG, Kobayashi N, *et al*. Phase formation and luminescence properties in Eu^{3+}-doped TiO_2 nanoparticles prepared by thermal plasma pyrolysis of aqueous solutions. Thin Solid Films, 2008, 516: 6640–6644
165 Zhang CN, Uchikoshi T, Li JG, Watanabe T, Ishigaki T. Influence of niobium doping on phase composition and defect-mediated photoluminescence properties of Eu^{3+}-doped TiO_2 nanopowders synthesized in Ar/O_2 thermal plasma. J Alloy Compd, 2011, 509: 8944–8951
166 Tachikawa T, Ishigaki T, Li JG, Fujitsuka M, Majima T. Defect-Mediated photoluminescence dynamics of Eu^{3+} doped TiO_2 nanocrystals revealed at the single-particle or single-aggregate level. Angew Chem Int Edit, 2008, 47: 5348–5352
167 Kaczmarek D, Domaradzki J, Borkowska A, *et al*. Optical emission from Eu, Tb, Nd luminescence centers in TiO_2 prepared by magnetron sputtering. Opt Appl, 2007, 37: 433–438
168 Zhao YM, Rabouw FT, Puffelen Tv, *et al*. Lanthanide-doped CaS and SrS luminescent nanocrystals: a single-source precursor approach for doping. J Am Chem Soc, 2014, 136: 16533–16543
169 Dethlefsen JR, Mikhailovsky AA, Burks PT, Døssing A, Ford PC. Lanthanide modification of CdSe/ZnS core/shell quantum dots. J Phys Chem C, 2012, 116: 23713–23720
170 Liu N, Xu L, Wang H, *et al*. Sensitization enhancement of europium in ZnSe/ZnS core/shell quantum dots induced by efficient energy transfer. Luminescence, 2014, 29: 1095–1101
171 Martín-Rodríguez R, Geitenbeek R, Meijerink A. Incorporation

and luminescence of Yb^{3+} in CdSe nanocrystals. J Am Chem Soc, 2013, 135: 13668–13671
172 Liu GK, Chen XY. Spectroscopic properties of lanthanides in nanomaterials. In: Gschneidner KA, Bunzli JCG, Pecharsky VK (eds.). Handbook on the Physics and Chemistry of Rare Earths. Amsterdam: Elsevier, 2007, 37: 99–170
173 Crosswhite HM, Crosswhite H. Parametric model for *f*-shell configurations. I. The effective-operator Hamiltonian. J Opt Soc Am B: Opt Phys, 1984, 1: 246–254
174 Carnall WT, Goodman GL, Rajnak K, Rana RS. A systematic analysis of the spectra of the lanthanides doped into single crystal lanthanum fluoride (LaF_3). J Chem Phys, 1989, 90: 3443–3457
175 Wybourne BG. Spectroscopic Properties of Rare Earths. New York: Interscience, 1965
176 Morrison CA, Leavitt RP. Spectroscopic properties of triply ionized lanthanides in transparent host crystals. In: Gschneidner KA, Eyring L (eds.). Handbook on the Physics and Chemistry of Rare Earths. Amsterdam: North-Holland, 1981, 5: 461–692
177 Chang NC, Gruber JB, Leavitt RP, Morrison CA. Optical spectra, energy levels, and crystal-field analysis of tripositive rare earth ions in Y_2O_3. I. Kramers ions in C_2 sites. J Chem Phys, 1982, 76: 3877–3899
178 Luo WQ, Li RF, Liu GK, Antonio MR, Chen XY. Evidence of trivalent europium incorporated in anatase TiO_2 nanocrystals with multiple sites. J Phys Chem C, 2008, 112: 10370–10377
179 Ma CG, Brik MG, Kiisk V, Kangur T, Sildos I. Spectroscopic and crystal-field analysis of energy levels of Eu^{3+} in SnO_2 in comparison with ZrO_2 and TiO_2. J Alloy Compd, 2011, 509: 3441–3451
180 Luo WQ, Fu CY, Li Rf, *et al*. Er^{3+}-doped anatase TiO_2 nanocrystals: crystal-field levels, excited-state dynamics, upconversion, and defect luminescence. Small, 2011, 7: 3046–3056
181 Kiisk V, Reedo V, Karbowiak M, Brik MG, Sildos I. Spectroscopic and crystal field study of Sm^{3+} in different phases of TiO_2. J Phys D Appl Phys, 2009, 42: 125107
182 Liu LQ, Chen XY. Energy levels, fluorescence lifetime and Judd–Ofelt parameters of Eu^{3+} in Gd_2O_3 nanocrystals. Nanotechnology, 2007, 18: 255704
183 Chen XY, Ma E, Liu GK. Energy levels and optical spectroscopy of Er^{3+} in Gd_2O_3 nanocrystals. J Phys Chem C, 2007, 111: 10404–10411
184 Chen XY, Luo ZD. Group-chain scheme analysis of the energy levels and magnetic properties of Er^{3+} in the $LiYF_4$ crystal. J Phys-Condens Mat, 1996, 8: 2571–2583
185 Reid MF. *f*-Shell empirical programs and examples. Private Communication.
186 Capobianco JA, Kabro P, Ermeneux FS, *et al*. Optical spectroscopy, fluorescence dynamics and crystal-field analysis of Er^{3+} in YVO_4. Chem Phys, 1997, 214: 329–340
187 Luo WQ, Li RF, Chen XY. Host-sensitized luminescence of Nd^{3+} and Sm^{3+} ions incorporated in anatase titania nanocrystals. J Phys Chem C, 2009, 113: 8772–8777
188 Walsh A, Da Silva JLF, Wei SH, *et al*. Nature of the band gap of In_2O_3 revealed by first-principles calculations and X-ray spectroscopy. Phys Rev Lett, 2008, 100: 167402
189 Fuchs F, Bechstedt F. Indium-oxide polymorphs from first principles: quasiparticle electronic states. Phys Rev B, 2008, 77: 155107
190 Bourlange A, Payne DJ, Egdell RG, *et al*. Growth of In_2O_3(100) on Y-stabilized ZrO_2(100) by O-plasma assisted molecular beam epitaxy. Appl Phys Lett, 2008, 92: 092117
191 Liang CH, Meng GW, Lei Y, Phillipp F, Zhang LD. Catalytic growth of semiconducting In_2O_3 nanofibers. Adv Mater, 2001, 13: 1330–1333
192 Dutta DP, Sudarsan V, Srinivasu P, Vinu A, Tyagi AK. Indium oxide and europium/dysprosium doped indium oxide nanoparticles: sonochemical synthesis, characterization, and photoluminescence studies. J Phys Chem C, 2008, 112: 6781–6785
193 Kim HK, Li CC, Barrios PJ. Erbium-doped indium oxide-films prepared by radio-frequency sputtering. J Vac Sci Technol A, 1994, 12: 3152–3156
194 Choi YG, Yu SM, Chung WJ. Local structural environment and photoluminescence of Er^{3+} ions doped in indium tin oxide nanopowder. Chem Phys Lett, 2008, 461: 290–293
195 Anticfidancev E, Aride J, Lemaitreblaise M, Porcher P, Taibi M. Emission-spectra and crystal-field calculation of europium-doped C-type In_2O_3 oxide. J Alloy Compd, 1992, 188: 242–245
196 Faucher MD, Dexpert-Ghys J. Crystal-field analysis of Eu^{3+} doped in cubic yttrium sesquioxide. Application of the electrostatic and angular overlap models. Phys Rev B, 1981, 24: 3138–3144
197 Tippins HH. Optical absorption and photoconductivity in band edge of beta-Ga_2O_3. Phys Rev, 1965, 140: A316–A319
198 Ueda N, Hosono H, Waseda R, Kawazoe H. Anisotropy of electrical and optical properties in beta-Ga_2O_3 single crystals. Appl Phys Lett, 1997, 71: 933–935
199 Geller S. Crystal structure of beta-Ga_2O_3. J Chem Phys, 1960, 33: 676–684
200 Nogales E, Mendez B, Piqueras J. Visible cathodoluminescence of Er ions in beta-Ga_2O_3 nanowires and microwires. Nanotechnology, 2008, 19: 035713
201 Vincent J, Guillot-Noel O, Binet L, *et al*. Electron paramagnetic resonance and optical spectroscopy of Er-doped beta-Ga_2O_3. J Appl Phys, 2008, 104: 033519
202 Xie HB, Chen LM, Liu YN, Huang KL. Preparation and photoluminescence properties of Eu-doped alpha- and, β-Ga_2O_3 phosphors. Solid State Commun, 2007, 141: 12–16
203 Wu ZP, Bai GX, Hu QR, *et al*. Effects of dopant concentration on structural and near-infrared luminescence of Nd^{3+}-doped beta-Ga_2O_3 thin films. Appl Phys Lett, 2015, 106: 171910
204 Wawrzynczyk D, Nyk M, Samoc M. Synthesis and optical characterization of lanthanide-doped colloidal Ga_2O_3 nanoparticles. Chem Phys, 2015, 456: 73–78
205 Layek A, Yildirim B, Ghodsi V, *et al*. Dual europium luminescence centers in colloidal Ga_2O_3 nanocrystals: controlled *in situ* reduction of Eu (III) and stabilization of Eu (II). Chem Mater, 2015, 27: 6030–6037
206 Liu YS, Luo WQ, Li RF, Chen XY. Spectroscopic evidence of the multiple-site structure of Eu^{3+} ions incorporated in ZnO nanocrystals. Opt Lett, 2007, 32: 566–568
207 Liu YS, Luo WQ, Li RF, Zhu HM, Chen XY. Near-infrared luminescence of Nd^{3+} and Tm^{3+} ions doped ZnO nanocrystals. Opt Express, 2009, 17: 9748–9753
208 Luo WQ, Li RF, Liu YS, Chen XY. Sensitized luminescence of Sm^{3+}, Eu^{3+}-codoped TiO_2 nanoparticles. J Nanosci Nanotechnol, 2010, 10: 1693–1698
209 Wang DD, Xing GZ, Gao M, *et al*. Defects-mediated energy transfer in red-light-emitting Eu-doped ZnO nanowire arrays. J Phys Chem C, 2011, 115: 22729–22735
210 Jin Y, Zhang JH, Lu SZ, *et al*. Fabrication of Eu^{3+} and Sm^{3+} codoped micro/nanosized $MMoO_4$ (M = Ca, Ba, and Sr) via facile hydrothermal method and their photoluminescence properties through energy transfer. J Phys Chem C, 2008, 112: 5860–5864
211 Kong JT, Zheng W, Liu YS, *et al*. Persistent luminescence from Eu^{3+} in SnO_2 nanoparticles. Nanoscale, 2015, 7: 11048–11054
212 Wu XJ, Meng FZ, Zhang ZZ, *et al*. Broadband down-conversion for silicon solar cell by ZnSe/phosphor heterostructure. Opt Express, 2014, 22: A735–A741
213 Wu XJ, Zhang ZZ, Meng FZ, *et al*. Core-shell-like Y_2O_3:[(Tb^{3+}-Yb^{3+}), Li^+]/CdZnS heterostructure synthesized by super-close-space sub-

limation for broadband down-conversion. Nanoscale, 2014, 6: 4745–4749
214 Zhu YS, Cui SB, Chen X, *et al*. Efficient energy transfer from inserted CdTe quantum dots to YVO_4:Eu^{3+} inverse opals: a novel strategy to improve and expand visible excitation of rare earth ions. Nanoscale, 2014, 6: 8075–8083

Acknowledgements This work was supported by the National Basic Research Program of China (2014CB845605), the Special Project of National Major Scientific Equipment Development of China (2012YQ120060), the National Natural Science Foundation of China (NSFC) (U1305244 and 21325104), the Chinese Academy of Sciences (CAS)/ State Administration of Foreign Experts Affairs International Partnership Program for Creative Research Teams, the CAS Cross-Disciplinary & Collaborative Research Team Program, and the Scientific Equipment Development Project of the CAS (YZ201210), the Key Project of Science and Technology of Fujian Province (2013H0060) and the NSF of Fujian Province for Young Scientists (2014J05070).

Author contributions Luo W and Chen X surveyed the literature and discussed the contents. Luo W, Liu Y and Chen X wrote the manuscript and designed the figures. All authors contributed to the general discussion and revision of the manuscript.

Conflict of interest The authors declare that they have no conflict of interest.

Wenqin Luo earned his BSc degree in chemistry from Xiamen University in China (2002). He received his PhD (2010) in materials physics and chemistry from Fujian Institute of Research on the Structure of Matter (FJIRSM), CAS. He joined the faulty at Huzhou University in 2014. His research interest focuses on the chemical synthesis and optical spectroscopy of lanthanide-doped nanoparticles.

Yongsheng Liu was born in Shandong, China. He earned his BSc degree (2001) in chemistry from Shandong Normal University. He received his MSc (2007) and PhD (2010) degrees in physical chemistry from FJIRSM, CAS. He joined Prof. Xueyuan Chen's group as an assistant professor in 2010 and was promoted to associate professor in 2012. Currently, his research interest focuses on the optical spectroscopy and bioapplications of lanthanide-doped nanomaterials.

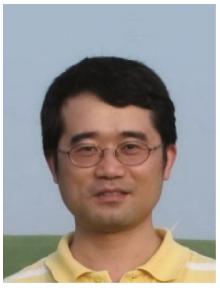

Xueyuan Chen earned his BSc degree from the University of Science and Technology of China (1993) and his PhD degree from FJIRSM, CAS (1998). From 2001 to 2005, he was a postdoctoral research associate at the Chemistry Division of Argonne National Laboratory, US Department of Energy, where he studied the photophysics and photochemistry of heavy elements. In 2005, he joined the faculty at FJIRSM, where he is currently professor and group leader in material chemistry and physics. His research focuses on the chemistry, optical spectroscopy and bioapplications of lanthanide-doped luminescent nanomaterials.

中文摘要 三价稀土离子掺杂半导体纳米晶具有独特的光学性能, 其在光电子器件、平板显示和荧光生物标记等方面的潜在应用前景, 获得了人们的普遍关注. 本文从材料制备、光谱性能、电子能级结构及能量传递机理等几个方面系统总结了近年来稀土掺杂半导体纳米晶的最新研究进展. 本文重点综述了通过湿化学方法把稀土离子掺杂进入半导体纳米晶晶格位置的合成策略、稀土离子在半导体纳米晶中的格位分布及半导体纳米晶到稀土离子能量传递机理. 同时, 还总结了近年来通过能级拟合计算来探索稀土在半导体纳米晶中的能级结构和晶体场参数的工作. 这些方面的研究对于深入理解稀土掺杂半导体纳米晶的光物理具有重要意义. 最后, 针对稀土掺杂半导体纳米晶未来的发展趋势与努力的方向作了进一步的前景展望.